2014

A PRACTICAL TOOL FOR THE DETERMINATION OF SURFACE STRESSES IN RAILROAD BEARINGS WITH DIFFERENT CONTACT GEOMETRIES AND LOAD CONDITIONS USING FINITE ELEMENT ANALYSIS

Michael A. Mason
masonma2@vcu.edu

A PRACTICAL TOOL FOR THE DETERMINATION OF SURFACE STRESSES IN

RAILROAD BEARINGS WITH DIFFERENT CONTACT GEOMETRIES AND LOAD

CONDITIONS USING FINITE ELEMENT ANALYSIS

A thesis submitted in partial fulfillment of the requirements for the degree of Master of Science in Mechanical and Nuclear Engineering at Virginia Commonwealth University.

by

MICHEAL ALLAN MASON
Bachelor of Science in Mechanical Engineering, Virginia Polytechnic Institute and State University, 2005

Director: CHARLES CARTIN
ASSISTANT PROFESSOR, DEPARTMENT OF MECHANICAL AND NUCLEAR ENGINEERING

Virginia Commonwealth University
Richmond, Virginia
December, 2014

Acknowledgements

I would like to express my appreciation and thanks to my advisor, Dr. Charles Cartin. You have been a great mentor that has always been extremely helpful with my research and the other requirements of my degree. A special thanks to my other committee members, Dr. John Speich, Dr. Parham Shahidi, and Dr. Brent Wilson for all your help throughout the process. Specially, the added guidance provided by Dr. Parham Shahidi as an academic mentor is greatly appreciated. I would also like to thank Amsted Rail Company, Inc. for funding this research and providing the opportunity for me to acquire my graduate degree in the midst of my career. Finally, I would like to express my endless appreciation for my loving wife, Tara Mason, who has continually shown her love and support for my goals, regardless of the adversities we had to face during the completion of my degree.

Table of Contents

List of Tables

List of Figures

Abstract

A PRACTICAL TOOL FOR THE DETERMINATION OF SURFACE STRESSES IN

RAILROAD BEARINGS WITH DIFFERENT CONTACT GEOMETRIES AND LOAD

CONDITIONS USING FINITE ELEMENT ANALYSIS

By Michael Allan Mason, M.S.

A thesis submitted in partial fulfillment of the requirements for the degree of Master of Science in Mechanical and Nuclear Engineering at Virginia Commonwealth University.

Virginia Commonwealth University, 2014

Major Director: Charles Cartin
Assistant Professor, Department of Mechanical and Nuclear Engineering

The connection between contact geometry and fatigue in tapered roller bearings utilized in the railroad environment is still of interest. Roller bearings for railroad applications are typically precision ground with crowned contact geometries to prevent edge loading of components. This normally results in completely elastic Hertzian contact stresses under standard railcar loads. However, under extreme load conditions, detrimental edge loading has been known to occur. It is proposed to develop a tool, using finite

element analysis, that can be utilized to optimize complex raceway crown geometries for severe applications.

A successful implementation of this tool is presented and validated using proven Hertzian contact theory. Correlation within 5% of the ultimate surface and subsurface stress magnitudes, using finite element modeling, in contrast with proven contact theory is achieved. In addition, analyses of other load conditions and contact geometries in order to illustrate the practical application of the tool are exhibited.

1. Introduction

Increasing freight car loads demand higher performance tapered roller bearings. As the stress state on railway bearing applications continues to increase, further advancement in the modeling tools and methods used for subsurface contact stress evaluations are needed. Heat treat specifications and contact geometries for railway bearings were originally developed for ideal load conditions. However, in railroad applications, tapered roller bearings are exposed to a vast range of load conditions that are seldom perfect. Moreover, when comparing global rail markets, there are often differences in bearing loads, railcar wear conditions, maintenance practices, and reliability versus utilization expectations. Advanced modeling techniques need to be developed by bearing designers in order to meet the specific needs of each individual rail market.

Prior research has shown that subsurface stresses, resulting from rolling contact, are the primary factor in the development of fatigue cracks in railway bearings. In addition, finite element modeling software has previously been used to analyze Hertzian contact stresses under rolling contact. Recent advancements in the technology and computational power of finite element methods allow engineers to numerically analyze more detailed simulations of complex geometries and biased load conditions in railway bearings. These improvements in the tapered roller bearing modeling methodology are necessary to

determine the material, heat treat specifications, and geometry required to meet the demands of specific railway bearing applications.

As an introduction to the work presented, the specific risks associated with some common railway bearing design and modeling assumptions will be evaluated. An exploratory list of these assumptions include: line versus point contact, load deflection factor, zero contact angle, rigid body assumptions, linear material behavior, neglect for overload, perfect geometric alignment, and uniform loading on the bearing. Emphasis will be placed on potential improvements in the theoretical and finite element prediction of surface and subsurface stresses in railway bearings under rolling contact with a review of prior research on the subject.

Hertzian contact stresses have been well documented and researched. There has also been significant improvement in finite element contact modeling technology since specific tapered roller bearings for railroad bearings were last modeled [1]. Hertzian theory will be used to validate finite element results for simple contact geometries with constant radii. This will be done through a comparison of subsurface stress magnitudes, subsurface stress locations, and the prediction of edge loading using the semimajor axis of the projected Hertzian contact ellipse. Prior work oversimplified the Hertzian contact problem in the railroad tapered roller bearing with crowned raceways by assuming a Hertzian line contact rather than Hertzian point contact [1].

Bearing failures continue to be an area of concern in the railroad industry. Although many improvements have been made over the years with regards to steel cleanliness, lubrications, heat treatment, and contact geometry; further optimization is

desired to improve bearing life in railcar applications. Bearings utilized in rail applications are exposed to a unique set of load conditions that require special consideration. Prior research has been conducted on specific automotive and aerospace bearing applications, with attention to the specific load conditions that arise in those environments. However, there is little work associated with the unique challenges faced in rail bearing design. Given the vast range of railcar designs, load conditions, environmental exposures, and remanufacturing standards, advanced bearing life prediction tools are required to optimize detailed designs. Whether design changes are required for cost reduction or design optimization for a particular application, finite element and other new design methodologies will be advantageous when attempting to meet the needs of the industry.

In the Introduction, classic bearing capacity and life prediction methods, as they pertain to various bearing applications, are reviewed while the relevance of surface and subsurface stresses are highlighted. Then, some issues that affect the accuracy of these methods are discoursed along with specifics of the novel modeling methodology nominated for further evaluation.

1.1   Surface Contact Stress in Fatigue Life Prediction and Railroad Tapered Roller Bearings

Common probabilistic bearing life prediction standards are based on the assumptions of proper alignment, even load distribution, and good lubrication. Bearing life is expected to be merely a function of material fatigue when taking these assumptions into consideration. More precisely, fatigue is expected to be initiated by subsurface Hertzian stresses below the surface of the raceway. Under perfect assumptions, the location and magnitude of these stresses can be calculated using classical Hertzian equations [2]. It should be noted that for line contacts, the limit of validity of Hertzian theory is exceeded whenever edge pressure occurs. Depending on the life prediction theory referenced, the most important stress is the maximum orthogonal shear stress [3], the maximum shear stress [4], or the von Mises stress [5]. Lundberg and Palmgren [3] suggest that the probability of survival of a bearing, S, can be related to an exponential relationship of maximum orthogonal shear stress, τ_o, the load cycles of repeated concentrated stress

$$N = A \left(\frac{1}{\tau_o}\right)^{c/e} \left(\frac{1}{aZ_ol}\right)^{1/e} (Z_o)^{h/e},$$ (1)

the depth of orthogonal shear stress, Z_o, and the stressed volume as

$$ln\frac{1}{S} \sim \frac{\tau_o^c N^e a l}{Z_o^{h-1}}. \tag{2}$$

Where the volume component in this relationship is a multiple of the semimajor axis of the Hertzian contact ellipse semi-length, a, the circumferential length of the raceway, l, and the depth of orthogonal shear stress by way of

$$V = aZ_o l. \tag{3}$$

Zaretsky alternatively suggests that the probability of survival can be related to the maximum shear stress τ_{max}, and the depth of the maximum shear stress Z_{max}, through

$$ln\frac{1}{S} \sim \tau_{max}^{ce} N^e a l Z_{max}. \tag{4}$$

Where the volume component becomes

$$V = aZ_{max}l \tag{5}$$

and the load cycles of repeated concentrated stress is

$$N = A \left(\frac{1}{\tau_{max}}\right)^c \left(\frac{1}{aZ_{max}l}\right)^{1/e}. \tag{6}$$

Furthermore, with regards to von Mises stress, Rinder suggests a probability of survival relationship

$$ln\frac{1}{S} \sim \frac{N^e}{Z_o^h} p_0^c \int_v \left(\frac{\sigma_e - S_u}{p_0}\right)^c dV, \tag{7}$$

where σ_e is the von Mises stress below the surface, S_u is the endurance strength of the material, and p_o is the maximum Hertzian contact pressure. It should be noted that if $(\sigma_e - S_u) < 0$ for any region of material within the specified volume, it will not be

included in the integral. Ioannides and Harris et al. [6] use a step function for this type of relationship between endurance strength and a stress related fatigue criterion. In equations (1), (2), (4), (6), and (7) the variables A, c, e, and h are all proportionality or material constants that must be evaluated empirically. Depending on the quality and type of bearing evaluated, these material and proportionality constants may need adjustment. In equations (3) and (5), the semimajor axis of the contact ellipse a is commonly replaced with the effective length of the raceway perpendicular to the direction of rolling for roller bearings. While the Lundberg and Zaretsky volumes are based solely on the depth of the maximum shear stress of concern, regardless of material properties, the Rinder volume takes into account the endurance limit of the material. For the Rinder fatigue life predictions, the integration covers the entire subsurface area stressed above the endurance limit of the material. This approach is more rational than the Lundberg and Zaretsky approach, given the random orientation of defects and inclusion types in bearing quality steel such as classified by Ebert [7]. This method is developed even further by Losche [5], Ioannides [6], and Harris [8] by removing the weight averaging of the depth of the critical stress peak. In addition, the inclusion of the endurance limit in the prediction of the probability of survival suggests that some bearing designs can achieve infinite life [6], contrary to the initial theories of Lundberg and Palmgren. However, there is still ongoing debate about this notion, as recently described by Zaretsky [9].

When comparing equations (2), (4), and (7), it can be seen that given the range and complexity of bearing life theories presented, advanced modeling tools such as finite element can be very helpful when optimizing bearing designs. Finite element models will

allow for simple determination of all the critical stresses used in the survival probability relationships previously discussed. Once the accuracy of the finite element modeling methodology for each basic design is validated, various stresses can be derived from strain results.

Current industry standards are still based on the early works of Lundberg and Palmgren, related to the maximum orthogonal shear stress [3,10]. As evidence of this, per the ANSI/ABMA standard [11], the basic fatigue rating life

$$L_{10} = a_2 a_3 \left(\frac{C_d}{P_r} \right)^p \tag{8}$$

is still calculated based on Lundberg and Palmgren theory, where C_d is the dynamic load capacity and P_r is the dynamic equivalent load. The load life adjustment factor

$$p = \frac{c - h + 1}{2e} \tag{9}$$

is 10/3 for roller bearings and

$$p = \frac{c - h + 2}{3e} \tag{10}$$

is 3 for ball bearings in the ANSI/ABMA standard. However, the load life adjustment factor in equation (10) ranges from 3 to 5, depending on the type of bearing and analysis referenced [3,8,10,12]. Synchronously, the life adjustment factor for special bearing properties a_2 and the life adjustment factor for operating conditions a_3 are both left up to the individual manufacturer's expertise. In addition, the standard suggests that an optimized adjustment factor for special bearing properties a_2 cannot be used in combination with an adjustment factor for operating conditions a_3 of less than 1; where

7

ideal lubricant and environmental conditions are required to achieve a a_3 value equal to 1. This would suggest that there is no expectation for design improvement in bearings that are not exposed to the ideal lubrication conditions described in the ANSI/ABMA standard. Conversely, the research presented in this thesis contradicts the ANSI/ABMA standard in that cognitive. As railroad bearings are often not exposed to ideal lubricant and environmental conditions, areas for improvement in special bearing properties, including detailed design geometry, will be studied. Commonly, bearing industry research suggests that a a_3 value of 1 requires that ε is greater than 1, at a minimum, where

$$\varepsilon = \frac{h}{R_{rms}}. \tag{11}$$

In equation (11), h is the minimum lubricant film thickness between raceway contacts and R_{rms} is the composite root mean square roughness of the contacting surfaces [13]. h is also a function of the contact pressure at the surface [14], which can be attuned through alterations to design geometry, as will be revealed in the following chapters.

As demonstrated above, for various bearing applications, classical fatigue life prediction tools and standards do not account for many of the complex loading scenarios that bearings are exposed to. Some of these complexities that are not accounted for when predicting fatigue life of bearings in the railroad industry are as follows: non-rigid support, foreign matter, residual stresses, internal clearances, alignment issues, inadequate lubrication conditions, and stress concentrations due to imperfect geometries. Railroad bearing applications also have the added complexity that the life of the product is not defined the same as in other industries. The definition of spalling remains consistent

8

across all industries and is defined in the Association of American Railroads Manual of Standards and Recommended Practices Section H-II [15]. However, an inconsistency with some other industries is that the fatigue life of the product in the rail industry is not always considered complete at the first evidence of fatigue spalling [11,15]. Although some industries allow for the remanufacture and restoration of bearing assemblies [12], the aggressive raceway fatigue regrinding practices allowed by the Association of American Railroads and in other global rail markets are not commonly allowed in other industries. These remanufacturing practices have a negative influence on subsurface stress magnitudes below the raceway surface. Alternatively, when resurfacing or replacing components of the bearing during reconditioning, the resulting impact on total bearing life, using the product law of probability, can be related as follows:

$$\left(\frac{1}{L_{10}}\right)^e = \left(\frac{1}{L_{ir}}\right)^e + \left(\frac{1}{L_{or}}\right)^e + \left(\frac{1}{L_{re}}\right)^e. \tag{12}$$

In equation (12), L_{ir} is the estimated reconditioned life of the inner ring, L_{or} is the estimated reconditioned life of the outer ring, and L_{re} is the estimated reconditioned life of the rolling elements where the Weibull slope e is the same for each of the individual components [2,12].

In addition to reconditioning practices, the low operating speeds found in some rail applications can result in additional surface friction if optimal lubricants are not used. For this reason, extreme pressure (EP) additives are commonly used [7]. However, in contrast, one advantage of low speed operation is that it results in low centrifugal and gyroscopic forces that can be ignored [16,17].

Although cylindrical roller bearings are still utilized in some rail bearing applications, the primary focus of this investigation is on the specific challenges associated with double row tapered roller bearing designs. These bearings are typically of similar composition to that shown in Figure 1, which commonly include one double row outer raceway or cup along with two cone assemblies that are assembled with tapered rollers. A spacer is used between the cone assemblies to control internal clearances within the bearing and these types of bearings typically operate as a sealed unit that is greased for the life of the application under the railcar. Recently, polymer cage geometries and clearances, utilized in cone assemblies, have been enhanced for optimized lubrication conditions and bearing life. Although tapered roller bearings in railcar applications commonly outlast the life of the wheel, there is still a need for improved modeling tools for optimization of designs, manufacturing processes, and failure analysis of discordant applications.
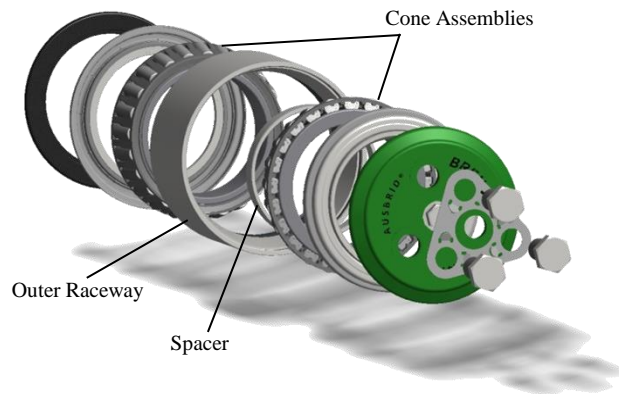
Figure 1: Double Row Tapered Roller Bearing for Railcar Applications

For specific rail applications, optimized heat treatment and geometry may be required to lower the stress state in the bearing. With regards to heat treatment, case hardening depths and retained austenite percentages can be matched to the subsurface

stress demands of the application [18]. A published guideline for case hardened bearings is to achieve a case that is approximately $3Z_o$-$4Z_o$ of the depth in equation (1) according to Harris and Yu [8]. When developing retained austenite specifications for a given application, dimensions stability has to be balanced with fatigue life due to stress induced austenite to martensite transformations [18]. In addition, bearing design configurations and geometries will be tailored as needed. For example, if it is known that a high degree of axle tilting will occur, crown geometry can be adopted accordingly and fatigue life can be increased. It is not uncommon in the rail industry to see the same particular bearing design utilized under very different load conditions, depending on which market it is operated. For instance, one market may load a bearing to 32 tonnes per axle while another market may load the exact same bearing to 40 tonnes per axle. Under the more extreme loading conditions, for the same basic bearing design, adjusted geometries or material properties may be desired by the customer for improved performance. In addition, reconditioning frequencies and standards will need to be developed depending on customer reliability versus utilization preferences. These issues again illustrate that improved bearing subsurface localized stress and life prediction tools will only make bearing designers more efficient at optimized tapered roller bearings to meet the needs of each individual customer.

1.2 Surface Stress Modeling Methods and Guidelines in Railroad Tapered Roller Bearings

Assuming ideal conditions, prior bearing research states that optimal bearing performance is achieved when the maximum loaded roller is operating under modified line contact conditions [2]. Where the total length of the semimajor axis of the roller and raceway contact ellipse $2a$, falls within the following bounds:

$$l \leq 2a \leq 1.5l. \tag{13}$$

Where l is the effective length of the roller. Furthermore, roller crown geometry, and the resulting nominal semimajor axis dimensions are typically established through multiplication of the dynamic load capacity C_d, of the bearing by some factor f_{RR}, established by the bearing manufacturer [2]. Therefore, the curvature ρ, for a roller or raceway profile can be established as

$$\rho = \frac{1}{f_{RR}C_d}. \tag{14}$$

As previously discussed, customary fatigue life prediction standards commonly ignore the details associated with line versus point contact stress concentrations and bearing life is calculated using the assumptions of Lundberg and Palmgren for most applications [3]. This approach allows for the adoption of a routine combination of point and line contact in regular designs. In the railroad environment, this guideline requires further investigation and given the wide range of uneven load conditions that can be

12

introduced, it is initially suggested that larger multiplication factors may be required for the most aggressive rail applications.

Equation (13) demonstrates that edge loading is commonly expected at the maximum loaded roller in typical designs. However, the magnitude and period of stress exposure during edge loading conditions, as Nagatani et al. [19] studies, needs to be evaluated by bearing designers. Typical Hertzian contact theory is not capable of predicting surface and subsurface stresses under edge loading conditions and finite element or other modeling methods will need to be used for these types of analyses. Nagatani suggests that the raceway should be divided into j number of laminas and that the life of each lamina should be calculated using the theories of Lundberg and Palmgren. As a result, Nagatani has proposed an alternative subsurface stress criterion and probability of survival relationship

$$ln\frac{1}{S} \sim \sum_{l_{eff}} \frac{\tau_{oj}^c N^e a_j l}{z_{oj}^{h-1}} \qquad (15)$$

that is based on the original theories of Lundberg and Palmgren; where the depth and location of the maximum orthogonal shear stress is calculated at each lamina location. This method can also be applied to the probability of survival relationships developed by Rinder, Zaretsky, Ioannides, and Harris. However, Nagatani warns that singularities may occur at the lamina near the edge of the contact in the von Mises or octahedral shear stress and uses orthogonal shear stresses for the stress criterion [19]. Using genetic algorithms, Kumar [20] takes this method a step further by using design optimization techniques to optimize cylindrical roller crown geometry. In Kumar's optimization problem, the purpose

13

is to maximize the objective function, which is equation (1). Furthermore, using a similar approach, Krzeminski-Freda et al. [21] studies the load distribution across the surface of a roller using an integral form of a modified contact capacity indicator.

If advanced modeling methodologies can be developed for stress analyses of specific applications, then some of the more recent bearing life prediction theories [5,6] can be used to estimate life, as these theories can account for peak stresses near the surface due to friction and edge loading surface pressure distributions. Losche [5] suggests that for ideal bearing applications, Hertzian subsurface stress calculations are the most significant stresses for failure prediction. Alternatively, under adverse loading conditions, surface Hertzian and frictional stresses are the critical factors necessary to predict failure.

Even with regards to basic Hertzian stress calculations, there is still an ongoing discussion regarding whether the orthogonal shear stress, maximum shear stress, or octahedral shear stress should be used for fatigue life prediction. This is evident in the survival probability relationships. Where the octahedral shear stress is different from the von Mises stress discussed above, by a factor of $\sqrt{3}/2$. Harris and McCool et al. [13] present a good overview of the advantages of each approach while Losche [5] and Harris [8] argue that octahedral shear stress or von Mises stress should be used. Furthermore, the resulting critical stress volumes necessary for fatigue life prediction associated with each approach have been evaluated by Harris [8]. The von Mises and maximum shear subsurface Hertzian stress magnitudes directly under the center of a symmetrical point contact are displayed in Figure 2. These stress distributions, calculated by Broszeit [22] using Hertzian theory, do not include the influence of any residual manufacturing or

14

frictional surface stresses. The theoretical prediction of these stresses will be evaluated

further in this paper along with a novel method of predicting these stresses in tapered roller

bearings using finite element analysis.
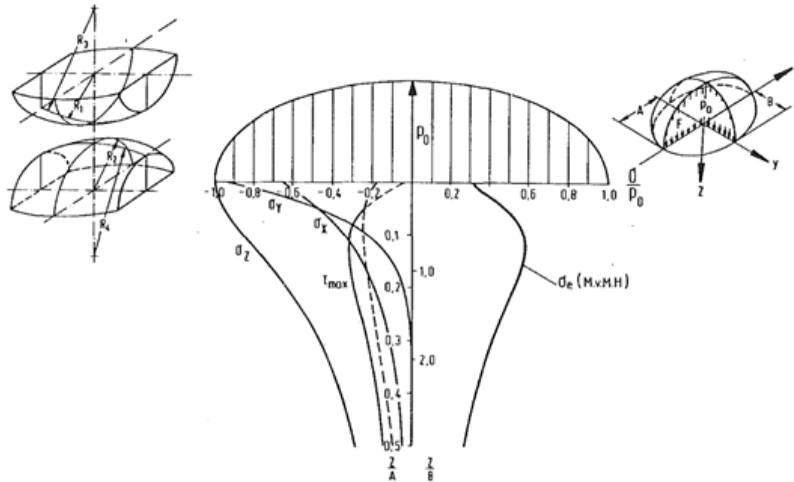
Figure 2: General Case of the Stressing of the Material in Two Crowned Bodies in Hertzian Point Contact Broszeit et al. [22]; Contact Radii Two Bodies in Point Contact (left), Subsurface Stresses Resulting from Hertzian Point Contact, Including Von Mises σ_e and Maximum Shear τ_{max} (center), and Surface Contact Pressure, Including Maximum Hertzian Contact Pressure p_o

Consideration of the distributions of loads to individual rollers must also be taken

into consideration before any of the subsurface stresses above can be calculated. The

Stribeck equations, as detailed in Appendix A, are commonly used to determine the

internal load distribution in bearings [2]. These equations can be used in combination with

Hertzian contact equations to calculate the surface contact ellipse dimensions for each

roller, as shown in Figures 3 and 4. When comparing the results in Figure 4 with equation

15

(13), industry standards would suggest that this example design has been optimized based

on the length of the semimajor axis of the contact ellipse.
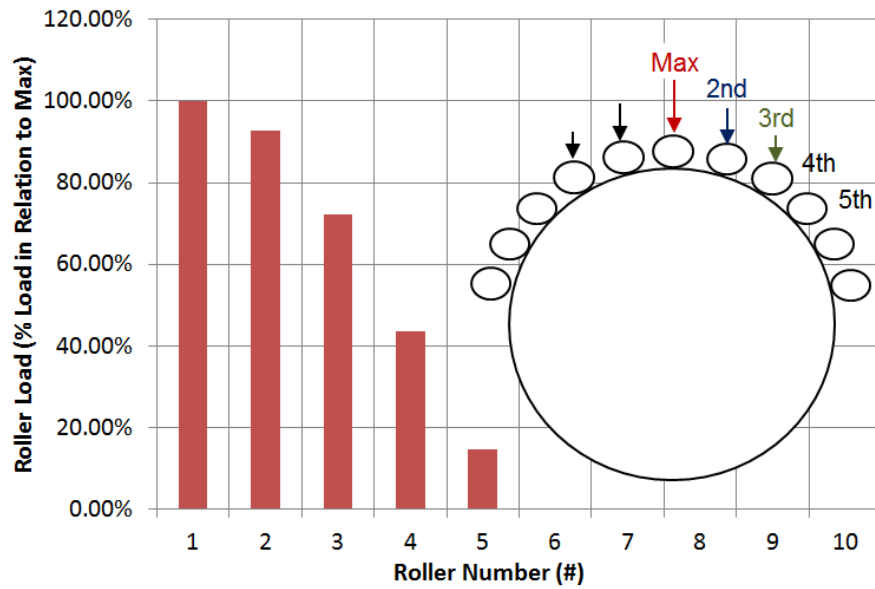
Figure 3: Roller Load Distribution According to Stribeck Equations for Hertzian Contact Ellipse Calculation in Figure 4
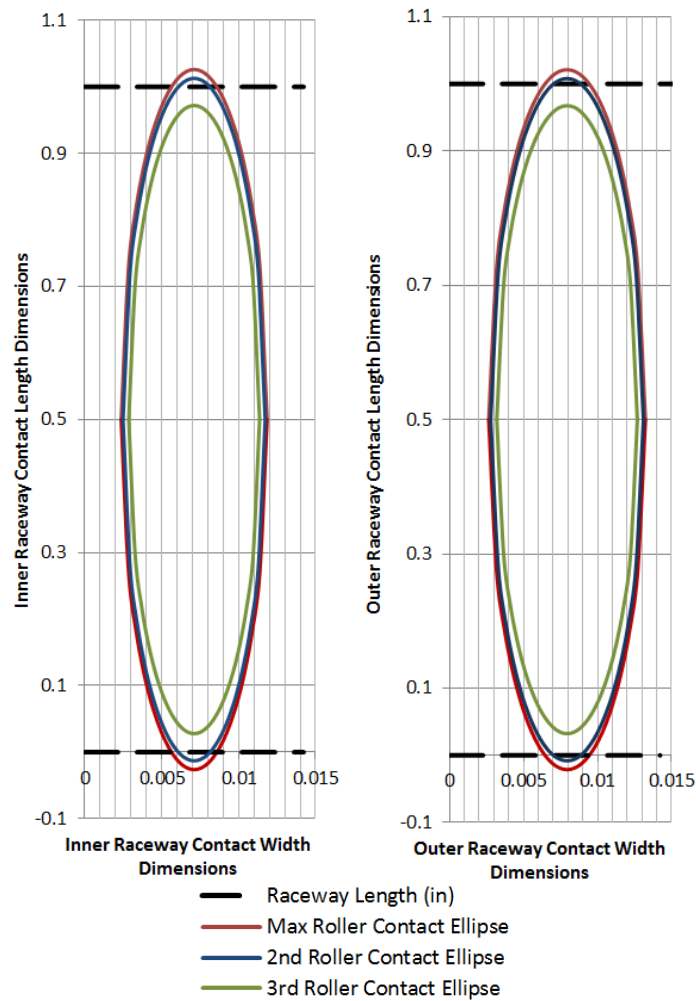
Figure 4: Contact Ellipse Dimensions According to Hertzian Contact Theory based on Roller Load Distribution Calculations in Figure 3

For more complicated roller load distribution scenarios, Andreason et al. [23] has developed an alternative method to calculate the load distribution in tapered roller bearings with misalignment using numerical methods. The need for crowned surfaces on tapered rolling elements to prevent fatigue and reduced bearing life under misalignment is supported by Andreason's analysis.

17

Additional complexities mentioned above, including residual stresses from manufacturing and surface friction effects will be needed to accurately determine the absolute stress state in railroad bearings. Residual stresses, resulting from manufacturing methods, typically have a positive effect on bearing performance [7] and can be measured using X-ray diffraction [18]. Broszeit [22] has studied the influence of residual and frictional stresses on the total surface and subsurface stress magnitudes below and at the raceway surface using superposition. One central finding from this analysis was that the entire area surrounding the contact must be studied in order to avoid reaching incorrect conclusions concerning the highest stress level in the material. In further research Broszeit and Zwirlein [24] confirm that the maximum equivalent von Mises stress is the preeminent stress parameter that should be used when analyzing complex subsurface contact stress patterns. Meanwhile, Broszeit and Zwirlein show that the maximum orthogonal shear stress is only useful to a limited extent in complex loading scenarios. In addition to frictional stresses below the surface, poor designs or frictional conditions within the bearing can result in roller skewing. Roller skewing, or angular shift of the roller, can then result in additional aggravation to the stress state of the raceway and cage [25]. Raceway and cage geometries are designed with the prevention of roller skewing in mind.

Lubrication also plays a vital role in reducing friction at the surface. Ioannides, Harris, and Yu illustrate how surface friction influences shear stress magnitudes below the surface with contour plots [6,8]. In general, good lubrication can minimize frictional power loss, assist in heat transfer, protect against corrosion, and prevent debris accumulation in the rolling contact path [14]. However, for comparative analyses of

different contact geometries and loading conditions, lubricant condition is often assumed to be constant and optimal for performance simulations. Only for detailed stress and fatigue life studies will all of the specific surface stresses associated with a particular lubrication condition need to be superimposed with rudimentary geometric stresses.

1.3   Overview of Novel Methodology Nominated for Tapered Roller Bearing Surface and Subsurface Stress Prediction

As introduced, numerical methods for the prediction of bearing raceway stresses have been previously studied and bearing life may be estimated based on the probability of survival relationship designated. The focus of the proposed methodology for bearing raceway surface and subsurface stress calculation in this paper will be on the minimum principle stress on the surface of the raceway as well as the subsurface stresses at the center of the elliptical contact, as illustrated in Figure 2. Theoretical prediction of surface and subsurface contact under common Hertzian contact will be discussed as well as special considerations related to tapered roller bearing designs in Chapter 2. Established bearing theory will then be used to validate a finite element method, proposed in Chapter 3, for the prediction of the stress state of the bearing raceway under a given load. Then, the finite element method developed will be used to analyze extraordinary load conditions that cannot be examined using established bearing theories and areas for future refinement of this work will be recommended in Chapter 4.

2. Hertzian Contact, Subsurface Stress Theory, and Tapered Roller Bearings

Hertzian contact theory may be used to calculate surface and subsurface stresses with the following assumptions: the yield strength of the material at the contacting surfaces is not exceeded, loading through the contact is perpendicular to the surfaces in contact, there is no shear loading at the surface, and the contact dimensions are small compared to the radii of curvature of the bodies in contact [2]. It should be noted that the theoretical Hertzian calculations presented in this chapter were used to validate a new finite element methodology, utilized to predict surface and subsurface contact stresses in railroad tapered roller bearings.

2.1 Surface Stress under Common Hertzian Contact

Figure 5 below shows two elliptical bodies in point contact with one another. In Figure 5, body I is the upper body and body II is the lower body in contact. The radius of curvature in plane 1 for body I is denoted as r_{I1} and the same radius of curvature naming convention is utilized for the other elliptical body and plane. When two elliptical bodies are in contact with each other, curvature sum and curvature difference are often used to define the contact [2]. Curvature difference

$$F(\rho) = \frac{\left(\frac{1}{r_{I1}} - \frac{1}{r_{I2}}\right) + \left(\frac{1}{r_{II1}} - \frac{1}{r_{II2}}\right)}{\Sigma \rho}, \tag{16}$$

is a function of curvature sum

$$\Sigma \rho = \frac{1}{r_{I1}} + \frac{1}{r_{I2}} + \frac{1}{r_{II1}} + \frac{1}{r_{II2}}. \tag{17}$$

In order to simplify equations (16) and (17), sometimes curvature

$$\rho = \frac{1}{r} \tag{18}$$

is used instead of radius of curvature, r.
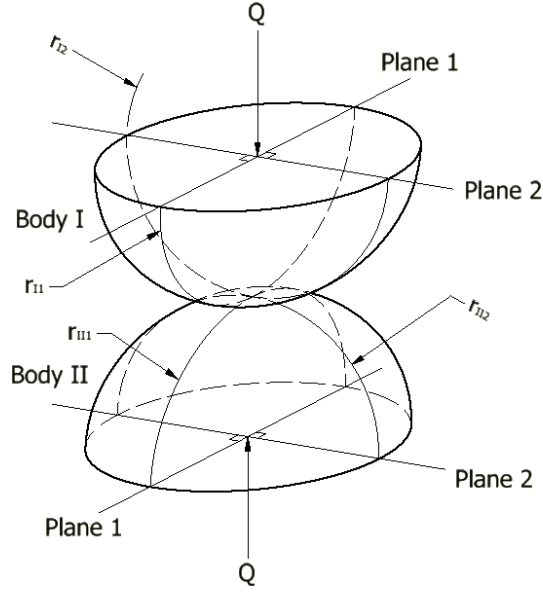
Figure 5: Two Elliptical Bodies in Contact with Different Radii of Curvature in each Plane

Using the Hertz assumptions previously discussed, curvature difference may also be expressed as

$$F(\rho) = \frac{(k^2+1)E\left(\frac{\pi}{2}\right)-2F\left(\frac{\pi}{2}\right)}{(k^2-1)E\left(\frac{\pi}{2}\right)} \tag{19}$$

where

$$F\left(\frac{\pi}{2}\right) = \int_0^{\frac{\pi}{2}}\left[1-\left(\frac{1}{k^2}\right)sin^2(\theta)\right]^{-1/2}d\theta \tag{20}$$

is the complete elliptic integral of the first kind,

$$E\left(\frac{\pi}{2}\right) = \int_0^{\frac{\pi}{2}}\left[1-\left(\frac{1}{k^2}\right)sin^2(\theta)\right]^{1/2}d\theta \tag{21}$$

is the complete elliptic integral of the second kind, and

23

$$k = {}^{a}/_{b} \tag{22}$$

is the elliptical eccentricity parameter for the given contact. In equation (22), a is the semimajor axis of the projected contact ellipse, as in equation (1), and b is the semiminor axis of the projected contact ellipse.

By assuming a value of the elliptical eccentricity parameter, the curvature difference can be calculated using the complete elliptic integrals in equations (20) and (21). This process can be repeated until an elliptical eccentricity parameter is found that results in a curvature difference equal to that calculated in equation (16). Once the elliptical eccentricity parameter for a given contact, as seen in Figure 5, is determined; the semimajor axis of the contact ellipse

$$a = \left[\left(\frac{2k^2 E\left(\frac{\pi}{2}\right)}{\pi} \right) \left(\frac{3Q}{2\sum\rho} \right) \left(\frac{1-\varepsilon_I^2}{E_I} + \frac{1-\varepsilon_{II}^2}{E_{II}} \right) \right]^{1/3}, \tag{23}$$

the semiminor axis of the contact ellipse

$$b = \left[\left(\frac{2E\left(\frac{\pi}{2}\right)}{\pi k} \right) \left(\frac{3Q}{2\sum\rho} \right) \left(\frac{1-\varepsilon_I^2}{E_I} + \frac{1-\varepsilon_{II}^2}{E_{II}} \right) \right]^{1/3}, \tag{24}$$

and the contact deformation

$$\delta = \frac{2F\left(\frac{\pi}{2}\right)\sum\rho}{2\pi} \left(\frac{\pi}{2k^2 E\left(\frac{\pi}{2}\right)} \right)^{1/3} \left[\left(\frac{3Q}{2\sum\rho} \right) \left(\frac{1-\varepsilon_I^2}{E_I} + \frac{1-\varepsilon_{II}^2}{E_{II}} \right) \right]^{2/3} \tag{25}$$

can be calculated for a particular roller load Q. In equations (23, 24, and 25), E_I and ε_I denote the elastic modulus and Poisson's ratio for elliptical Body I respectively. Similarly, E_{II} and ε_{II} denote the elastic modulus and Poisson's ratio for elliptical Body II in contact.

Once the dimensions of the elliptic contact region have been established for a roller under a contact normal load Q, the maximum compressive stress on the surface $\sigma_{z\,max}$, which occurs at the center of the Hertzian contact, can be calculated as

$$\sigma_{z\,max} = \frac{3Q}{2\pi ab}. \tag{26}$$

Additionally, the normal compressive stress at other locations on the surface inside the elliptical Hertzian contact region is often of interest and can be determined using

$$\sigma_z(z = 0) = \sigma_{z\,max}\left[1 - \left(\frac{x}{a}\right)^2 - \left(\frac{y}{b}\right)^2\right]^{1/2}. \tag{27}$$

It should be noted that equations (23) – (27) assume infinitely continuous radii of curvature in all directions. It is know that bearing raceways and rollers are not infinitely continuous, as raceways commonly have a finite length. Therefore, roller race contact edge loading conditions often occur in traditional designs, as presented in equation (13). One published guideline associated with designing roller bearings for this condition, as shown in equation (14) and discussed in the introduction, can be assessed further using finite element methods.

2.2 Subsurface Stress under Common Hertzian Contact

Once surface contact stresses are established for a given contact geometry, subsurface stresses may be calculated using the methods provided by Johnson [26]. As described by Johnson, subsurface stresses along the z-axis, directly below the center of the contact (Figure 6), may be calculated using the semimajor axis of the contact ellipse, the semiminor axis of the contact ellipse, the maximum compressive stress on the surface of the contact, and an eccentricity parameter defined as

$$e = \sqrt{1 - \frac{b^2}{a^2}}. \tag{28}$$
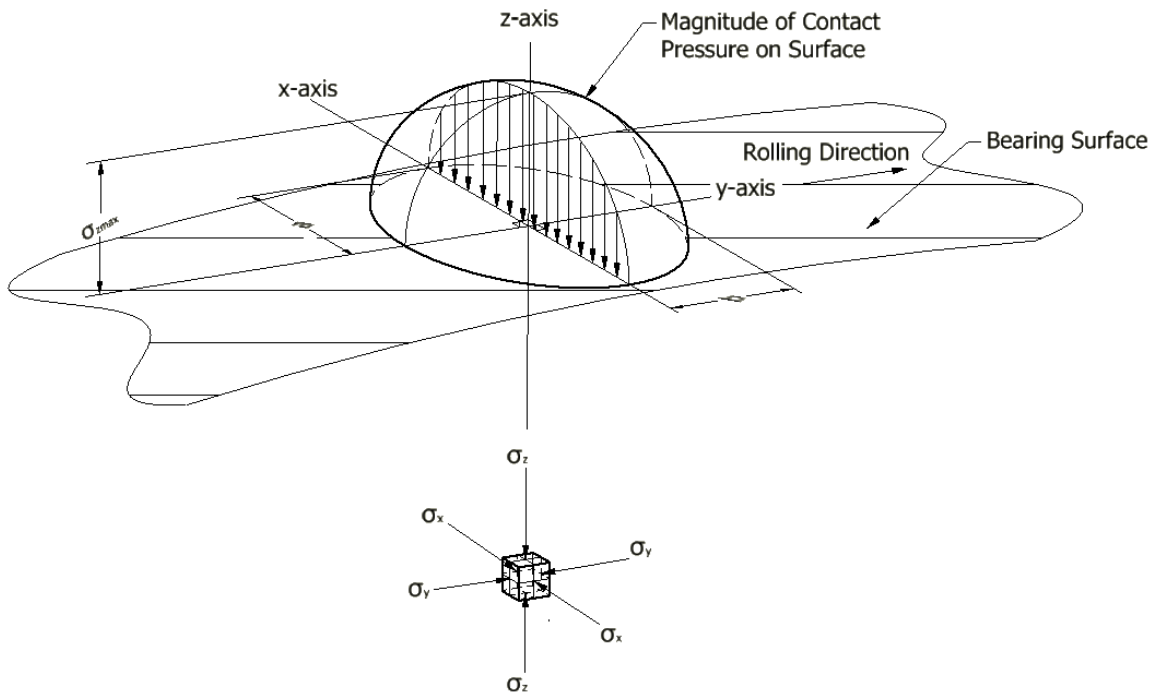
Figure 6: Subsurface Stress on Element below Bearing Surface Located on z-axis, directly below the Center of the Contact

Where subsurface principle stress in the z-direction, may be demarcated as

$$\sigma_z(z < 0) = -\sigma_{zmax}\left(\frac{b}{e^2 a}\right)\left(\frac{1-T^2}{T}\right) \qquad (29)$$

with

$$T = \sqrt{\frac{b^2+z^2}{a^2+z^2}}. \qquad (30)$$

Meanwhile, subsurface stress in the x-direction,

$$\sigma_x = \sigma_{zmax}\left(\frac{2b}{e^2 a}\right)\left(-\frac{1}{2}(1-T) + \frac{z}{a}(F(\emptyset) - E(\emptyset)) + \varepsilon\left[1 - \left(\frac{a^2 T}{b^2}\right) + \right.\right.$$

$$\left.\left.\frac{z}{a}\left(\left(\frac{a^2}{b^2}\right)E(\emptyset) - F(\emptyset)\right)\right]\right) \qquad (31)$$

and subsurface stress in the y-direction,

$$\sigma_y = \sigma_{zmax}\left(\frac{2b}{e^2 a}\right)\left(\frac{1}{2}(1+T) - \left(\frac{a^2 T}{b^2}\right) + \frac{z}{a}\left(\left(\frac{a^2}{b^2}\right)E(\emptyset) - F(\emptyset)\right) + \right.$$

$$\left. +\varepsilon\left[-1 + T + \frac{z}{a}(F(\emptyset) - E(\emptyset))\right]\right) \qquad (32)$$

are calculated using incomplete elliptic integrals of the first and second kind. In equations (31) and (32), ε is the Poisson's ratio of the material of interest,

$$F(\emptyset) = \int_0^\emptyset \left[1 - \left(1 - \frac{1}{k^2}\right)sin^2(\theta)\right]^{-1/2} d\theta \qquad (33)$$

is the incomplete elliptic integral of the first kind, and

$$E(\emptyset) = \int_0^\emptyset \left[1 - \left(1 - \frac{1}{k^2}\right)sin^2(\theta)\right]^{1/2} d\theta \qquad (34)$$

is the incomplete elliptic integral of the second kind, where

27

$$\emptyset = \cot^{-1}\left(\frac{z}{a}\right).$$
(35)

Once the subsurface principle stresses are known, the maximum shear stress below the surface of the contact may easily be calculated as

$$\tau_{max} = \frac{1}{2}(\sigma_1 - \sigma_3)$$
(36)

where σ_3 is equal to σ_z and σ_1 is equal to σ_x or σ_y depending on which stress has a larger magnitude at a particular depth below the contact surface. In addition, the von Mises equivalent stress may also be calculated below the surface using

$$\sigma_e = \frac{1}{\sqrt{2}}\sqrt{\left(\sigma_x - \sigma_y\right)^2 + \left(\sigma_y - \sigma_z\right)^2 + (\sigma_z - \sigma_x)^2 + 6\left(\tau_{xy}^2 + \tau_{yz}^2 + \tau_{zx}^2\right)}$$
(37)

Observing that the stresses in equations (29), (31), and (32) are principle stresses calculated along the z-axis, directly below the center of the contact, equation (37) may be simplified further as

$$\sigma_e = \frac{1}{\sqrt{2}}\sqrt{\left(\sigma_x - \sigma_y\right)^2 + \left(\sigma_y - \sigma_z\right)^2 + (\sigma_z - \sigma_x)^2}$$
(38)

along the z-axis in Figure 6.

2.3 Special Considerations Related to Hertzian Contact Calculations in Tapered Roller Bearings – Bearing Geometry

Hertzian contact stress theory for two elliptical surfaces in contact has been reviewed. Subsequently, some of the specific concepts related to stress prediction in tapered roller bearings should be further considered. Two concepts related to tapered roller bearing geometry, important for initiation of stress calculations, include crown height relationships and the radius of curvature of a tapered surface. Both of these geometric concepts, related to tapered roller bearing design, will be discussed further below.

Prior to introducing details related to the macrogeometry of tapered roller bearing designs, it is helpful to outline some common nomenclature associated with these types of bearings. The naming conventions commonly used for tapered roller bearing features, referenced throughout this paper, are offered in Figure 7 below.
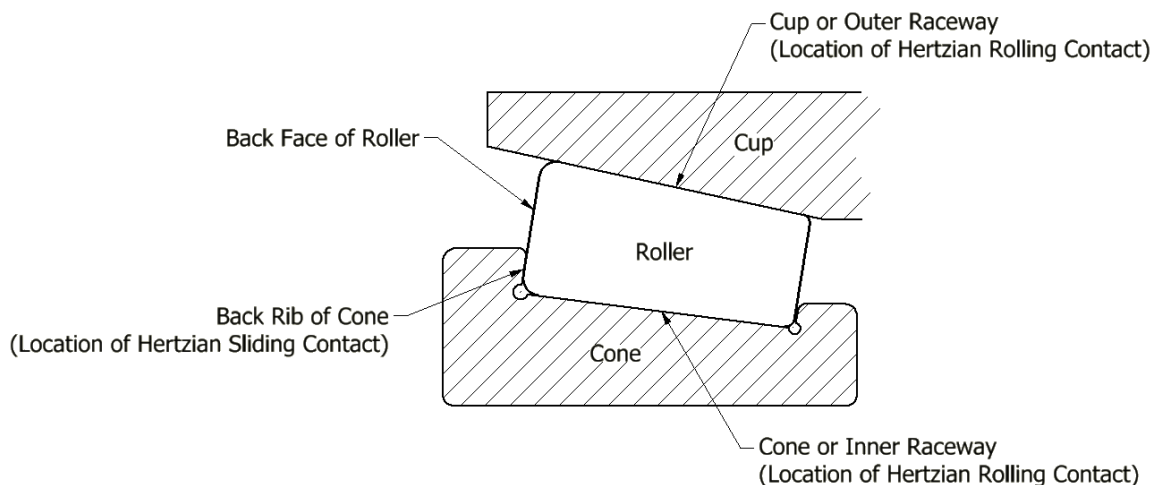
Figure 7: Tapered Roller Bearing Raceway Geometry Nomenclature

It is normal in the tapered roller bearing industry to use crown height, instead of radius of curvature or curvature, to identify raceway and roller elliptical contact profile geometry. Prior to calculating the curvature sum and curvature difference in equations (16) and (17), the radius of curvature of the raceway or roller contact surface must be known. By utilizing the crown height h_c and center span crown length l_c in combination with the intersecting chord theorem

$$r = \frac{h_c}{2} + \frac{(l_c)^2}{8h_c},$$

as illustrated in Figure 8 and discussed by Glaister [27], the radius of curvature on the raceway of the component of interest can be determined. The center span crown length is generally specified by the individual bearing manufacturer and the derivation of equation (39) may be found in Appendix B. If the radius of curvature of the crown geometry is provided for the specific bearing design being analyzed, this relationship may not be required. However, it is helpful to understand the association of crown nomenclature as it is commonly encountered when discussing detailed roller bearing design.
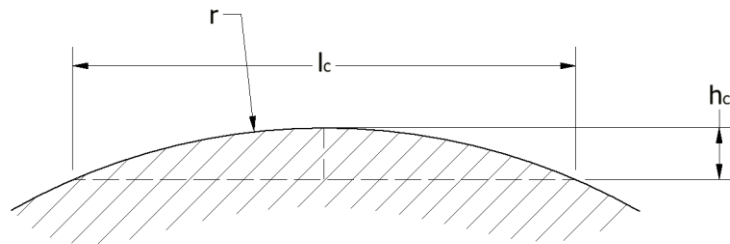
Figure 8: Relationship between Radius of Curvature, r, and Crown Height, h_c

With regards to tapered roller bearing macrogeometry, the radius of curvature used

for the cone raceway diameter, at the center of the raceway, may be approximated as

$$r_i = \frac{d_{iLE} - (l_{body}) \, \text{SIN}(\theta_i)}{2} \tag{40}$$

and the radius of curvature of the central cup raceway diameter may be approximated as

$$r_o = \frac{d_{oLE} - (l_{body}) \, \text{SIN}(\theta_o)}{2}. \tag{41}$$

Where d_{iLE} is the large end diameter of the cone and θ_i is the angle of the cone raceway.

Similarly, d_{oLE} is the large end intersection diameter between the cup and the back face of

the roller and θ_o is the angle of cup raceway. These design parameters, used to initiate

calculations related to Hertzian contact stress predictions in tapered roller bearings, may be

seen in Figure 9.
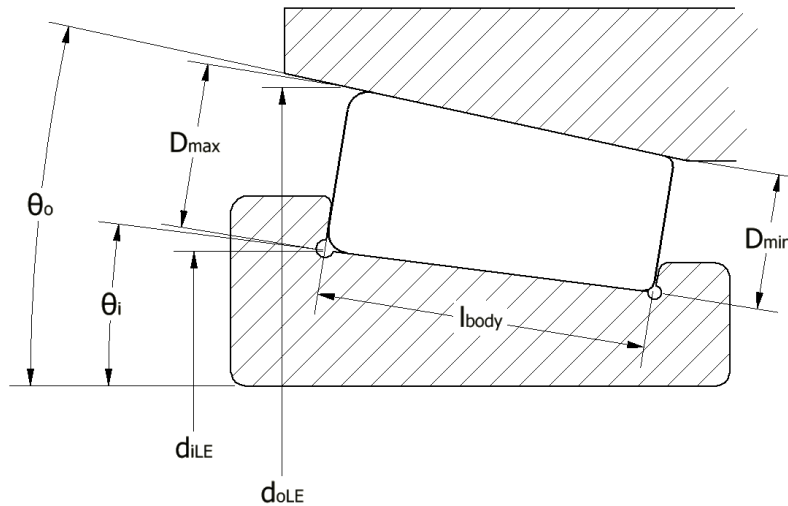
Figure 9: Tapered Roller Bearing Macrogeometry for Radius of Curvature Calculations

In addition to the inner and outer raceway, the radius of curvature related to the average roller diameter, may be approximated as

$$r_r = \frac{D_{max} + D_{min}}{4};$$ (42)

where D_{max} is the large end roller diameter and D_{min} is the small end roller diameter of the specific roller of interest. To further identify the significance of the equations above for tapered roller bearing analyses, equations (39) - (42) may be used as a starting point for the theoretical estimation of surface contact stresses by means of equations (16) - (27).

2.4 Special Considerations Related to Hertzian Contact Calculations in Tapered Roller Bearings – Roller and Raceway Forces

The balance of the forces between the roller and raceway components in the tapered roller bearing system must be understood in order to have confidence in surface and subsurface stress predictions. Once the maximum force on an individual roller is estimated using the Stribeck equations [2] or other method, the resultant force on the cup raceway, cone raceway, and cone back rib may be calculated (Figure 7). The normal force between the cup and tapered roller may be related to the force applied to the outer diameter of the cup, in the plane of symmetry of the roller, through the relationship

$$Q = \frac{Q_{max}}{\cos(\theta_o)}.$$ (43)

This demonstrates that the radial component of the force

$$Q_r = Q * \cos(\theta_o)$$ (44)

on the roller in the top dead center position of the bearing, which is parallel with the load applied to the outer diameter of the cup in Figure 10, is equal to aforesaid cup outer diameter load Q_{max}. Furthermore, the component Q_r, which is shown to be equivalent to Q_{max}, is assumed to be identical to the maximum individual roller load calculated using the Stribeck equations in the analyses that follow.
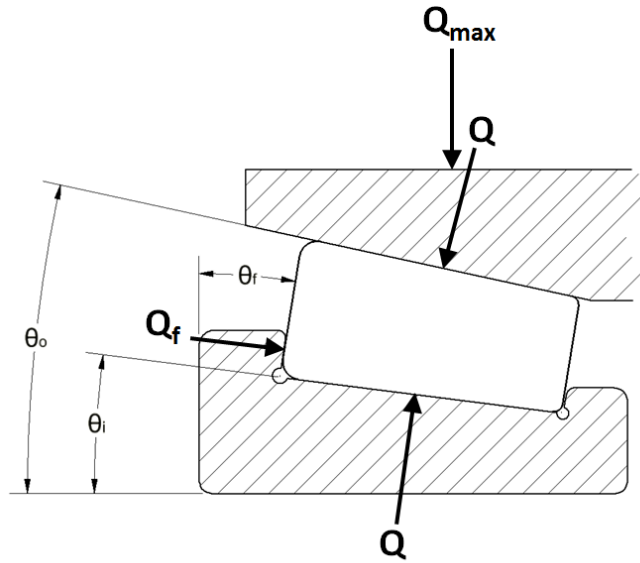
Figure 10: Forces on Tapered Roller in Bearing

It can be shown, as demonstrated in Appendix C, that the force transferred from the cup to the roller is the same as that transferred from the roller to the cone raceway in common tapered railroad bearing geometries if the relationship between the angles in Figure 10 is:

$$\theta_f = \frac{\theta_o + \theta_i}{2}. \tag{45}$$

Otherwise, the relationship between the force transmitted from the cup to the roller, Q, and from the roller to the cone, Q_i, is:

$$Q_i = Q \frac{\cos(\theta_o - \theta_f)}{\cos(\theta_f - \theta_i)} \tag{46}$$

which is

$$Q_i = Q \, \text{COS}(\theta_o - \theta_i) \tag{47}$$

when the flange reaction angle θ_f is assumed to be equal to the cone angle θ_i. Moreover,

the force between the roller and the back rib of the cone may be calculated as

$$Q_f = \frac{Q(\text{SIN}(\theta_o) - \text{COS}(\theta_o) \, \text{TAN}(\theta_i))}{\text{COS}(\theta_f) + \text{SIN}(\theta_f) \, \text{TAN}(\theta_i)} \tag{48}$$

for verification of finite element forces.

3. Hertzian Contact and Subsurface Stress Finite Element Modeling in Railroad Tapered Roller Bearings

The thorough review of Hertzian contact theory presented in Chapter 2 will be compared with two different finite element modeling methodologies used to study a sample railroad tapered roller bearing geometry. The primary differences in the two modeling methods presented include the mesh scheme utilized and the inclusion of the contact between the large end face of the roller and the back rib of the cone in the model. The advantages and disadvantages of each modeling methodology will be discussed and results will be compared to the theoretical predictions of Chapter 2. All finite element analyses conducted were performed using Ansys 15.0 Mechanical software developed by Ansys, Inc. Prior to the detailed explanation of the novel finite element modeling methods selected, prior work on the use of finite element as a surface and subsurface stress prediction tool will be reviewed.

3.1 Finite Element as a Surface and Subsurface Stress Prediction Tool

As shown in equation (15) by Nagatani, some edge loading prediction techniques divide the roller race surface up into lamina for calculation of surface and subsurface stresses in the bearing [19]. Finite element analysis is another method that can be used to subdivide the contacting surfaces and bodies into subdomains for simplification of stress calculations. One source [28] suggests that for a Hertzian stress finite element model of a tapered roller bearing, a mesh density around the contact surface that is equal to or less than one half of the semiminor axis of the Hertzian contact ellipse should be used. Another study [29] has compared the analytical and computational finite element Hertzian subsurface stresses in a turbine blade with reasonably accurate results. Surprisingly, most of the prior finite element work specifically related to the Hertzian stress prediction in roller bearings assume line contact profiles and do not take into account crown profile tolerances. Many of these studies appear to show singularities near the edge of the contact, as would be expected with this type of assumption. An example of the results of one analysis conducted by Dick et al. [1] on a railroad tapered roller bearing with and without roller crown is shown in Figure 11. It can be seen that high stress peaks occur at the edges of the contact when crown geometry is not included in the analysis.
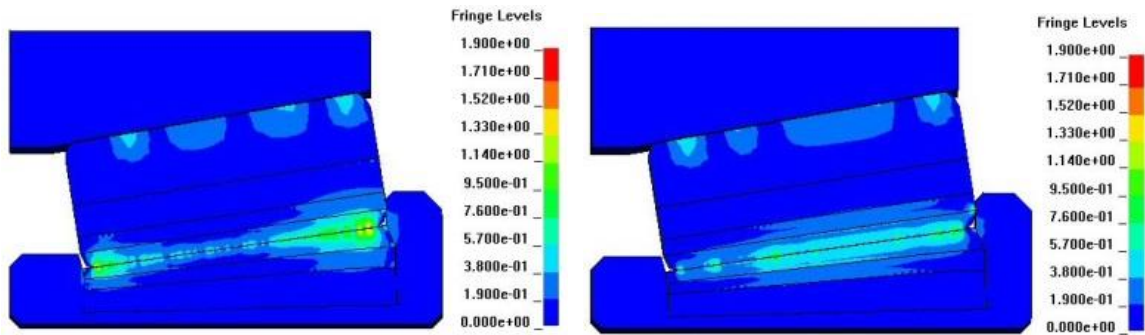
Figure 11: Comparison of von Mises Stress (MPa) of Bearing Models with (left) and without (right) a Raceway and Roller Crown [1]

As with theoretical Hertzian subsurface stress calculations, the roller load distribution in the bearing must be established before individual subsurface stresses under each roller can be analyzed using finite element. Guo [16] notes discrepancies in the load deflection factors used in published theoretical models which are frequently used as a foundation for roller load distribution calculations. In particular, it is noted that experimental results differ significantly from theoretical load deflection relationships based on Hertzian contact theories and that finite element methods may be able to provide a more accurate prediction of bearing stiffness. This difference is noted specifically when common raceway thicknesses, seen in available commercial products, are used in simulations. Alternatively, bearing stiffness agreement with published theories is achieved if unrealistically thick and rigid raceways are modeled. Issues related to theoretical roller load prediction are beyond the scope of this paper and it will be assumed that the Stribeck equations, as detailed in Appendix A, are valid.

As mentioned in the introduction, continued advancement in the computational power of computers and finite element capabilities allow for more complex simulations. If

38

modeled properly, the following advantages in the surface and subsurface stress prediction in tapered roller bearings for railroad applications will be recognized using finite element analysis:

1. Edge loading sensitivity, due to design or adverse application conditions can be studied.

2. Discontinuities and defects resulting from application damage or reconditioning practices can be analyzed.

3. Rigid support assumptions, commonly used in bearing theory, can be evaluated. With regard to railcar applications exactly, axle and adapter deflections can be included in models.

4. Rigid body assumptions used for roller load distribution calculations or raceway load distribution calculations for multiple row bearings can be evaluated.

5. The effect of aggressive and uneven loads on raceways in a multiple row bearing can easily be evaluated by changing input load conditions.

6. Non-linear material properties can effortlessly be included in models.

7. A complete picture of the three dimensional stress state of a given design and load combination can be considered for potential areas of improvement.

8. Detailed models will allow for easy transition into sensitivity studies of different design variables.

3.2 Primary Method for Hertzian Contact and Subsurface Stress Finite Element Modeling

To validate the accuracy of the proposed finite element technique for railroad tapered roller bearings, a primary finite element model was developed for comparison with theoretical surface and subsurface stress predictions. Standard crown geometries, with one continuous radius of curvature, and a roller load that would not result in edge loading were employed.

The crown of the roller and raceway contact geometries were positioned, as much as possible with the bearing geometry modeled, so that they would contact the center of the opposing crown surface. As perceived in Figure 12, the center point of each crown was identified with a point in the computer aided design model. It was not plausible to perfectly center the roller crown with the inner raceway crown without creating interference with the back rib of the cone. During initial iterations of the finite element method, the additional complexities associated with the extra contact region created by roller contact with the back rib of the cone were avoided. Therefore, a negotiated lateral location of the tapered roller in the bearing modeled was employed, by placing the roller directly in between the front and back rib of the cone. As discussed further below, the lateral position of the roller was constrained in this location during the entire primary simulation, using contact settings.
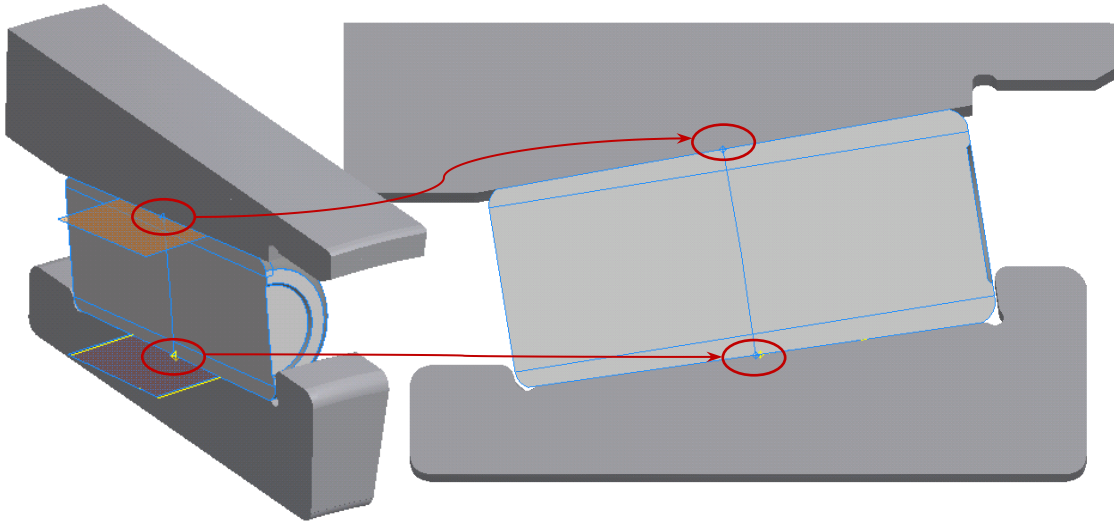
Figure 12: Lateral Position of Tapered Roller in between Inner and Outer Raceways with Crown Geometry Centered as much as Possible in Primary Finite Element Model

All of the components in the finite element simulation where modeled using the material properties of standard structural steel and nonlinear material effects were not included in the model. Material properties associated with the structural steel used in this simulation are shown in the Appendix D, Table 4.

A contact region was setup between the roller and cup raceway with frictionless contact behavior [30] to prevent interpenetration and allow for contact compatibility while permitting the two solids to slide relative to each other. Frictionless contact behavior was also modeled between the roller, cone raceway, and cone back rib surface, as shown in Figure 13. All contacts were modeled using the Augmented Lagrange formulation with asymmetric behavior [30]. The Augmented Lagrange formulation uses integrated point detection between finite element nodes and an augmented term in the contact formulation to reduce sensitivity to the magnitude of the contact stiffness in each contact region.

Meanwhile, asymmetric behavior assigns one surface in a contact region as the contact surface and the other surface in the same contact region as the target surface where only the contact surface is constrained from interpenetration of the target surface. As mentioned above, the frictionless contact between the cone back rib and roller interface treatment setting was set to "adjust to touch" in order to keep the roller crown centered in the middle of the front and back rib of the cone. The "adjust to touch" setting builds a rigid region between two surfaces, eliminating any gap that may exist in the computer aided design model. Centering of the roller crown in this location is not an exact simulation of common tapered roller bearing behavior, as previously discussed. However, this allowed for initial finite element simulation results to be simplified for comparison with theoretical Hertzian predictions and the results of this method will also be compared with another modeling technique that includes contact with the back rib of the cone in Chapter 3.5.

A contact stabilization force was also used in order to prevent rigid body motion of the outer raceway, inner raceway, and roller. Stabilization is generally only deemed necessary during initial substeps of the analysis before contact is established in all regions of the model. However, the influence of the stabilization force on the strain energy transmitted through each contact is constant throughout the entire simulation and therefore every substep of the analysis. Given that the primary analysis of the tapered roller bearing is static structural in nature, the pseudo velocity V_n is calculated by the finite element software based on the number of substeps specified and the initial gap between contacting

surfaces. This is used along with a contact stabilization factor f_d to calculate the dampening force

$$F_d = \int f_d V_n \, dA_c \tag{49}$$

over the contact region A_c. Caution was taken to reduce the contact stabilization factor as much as possible in order to achieve the best correlation between finite element and theoretical Hertzian contact surface stress predictions. After several iterations, a contact stabilization factor equal to one was determined to provide acceptable results as will be discussed further during the presentation of finite element analysis results.
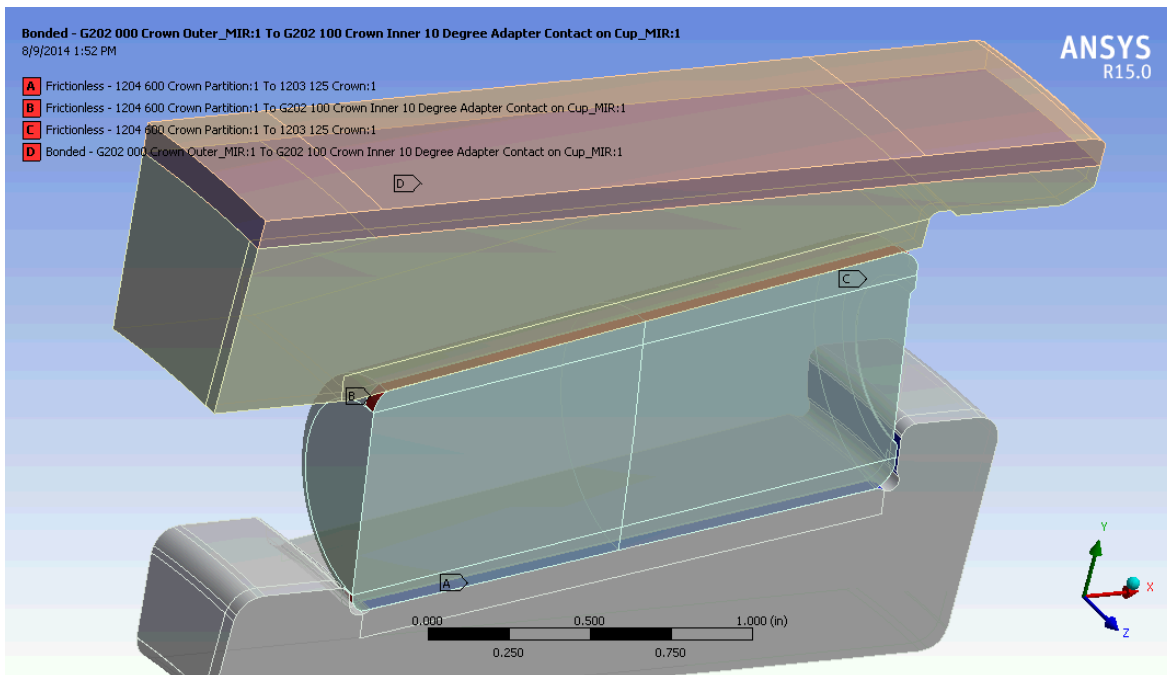
Figure 13: Areas of Contact in the Primary Finite Element Model

For the primary simulation, a hex dominant mesh was used with 15,128,613 nodes and 10,771,193 elements (Figure 14). The mesh was constructed by means of contact sizing with a relevance setting of 100% for the raceway roller contacts and a relevance setting of 20% for the roller large end contact with the cone back rib. Additionally, a mesh refinement level of three was used on the partitioned surfaces of the roller and raceways, as shown below, near the contact surfaces between the roller and raceways (Figure 14). Edge sizing was also used on all contacting edges of the roller and raceway contacts, with a fixed element size of .002 inches. Furthermore, a subsurface refinement was employed along the subsurface centerline of the crowned surface of the roller near both the inner and outer raceway crown contacts with a refinement level of two, as shown in Figure 15.

.
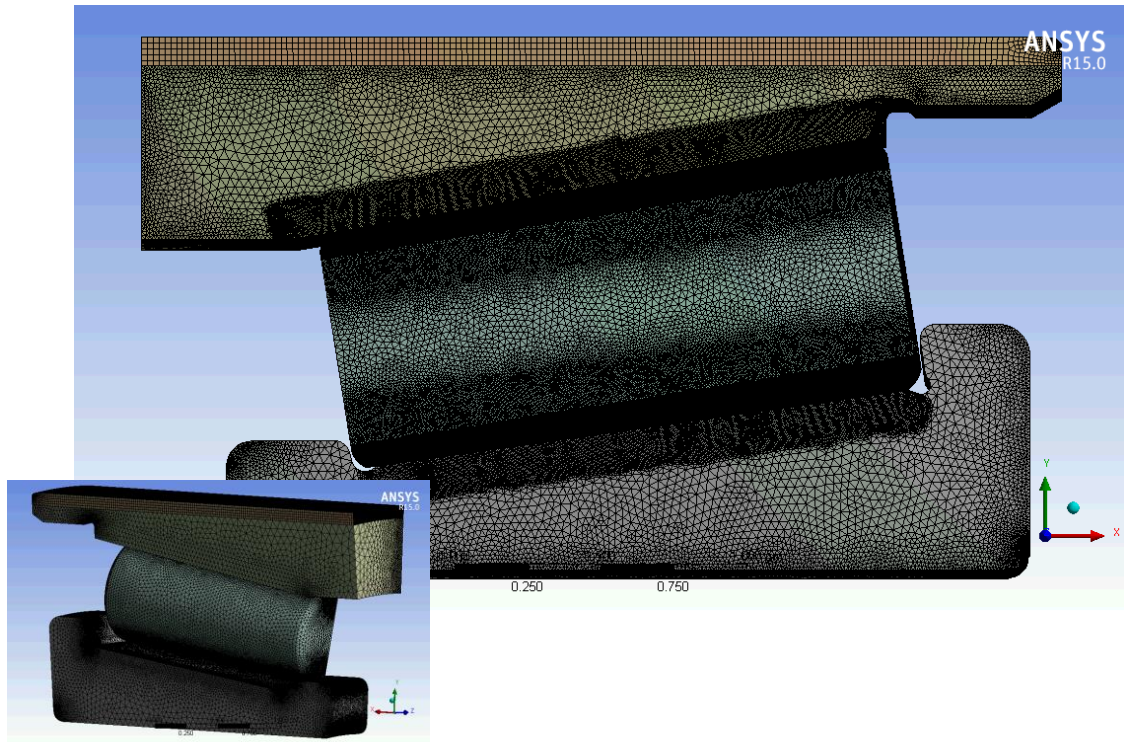
Figure 14: Mesh in the Primary Finite Element Model
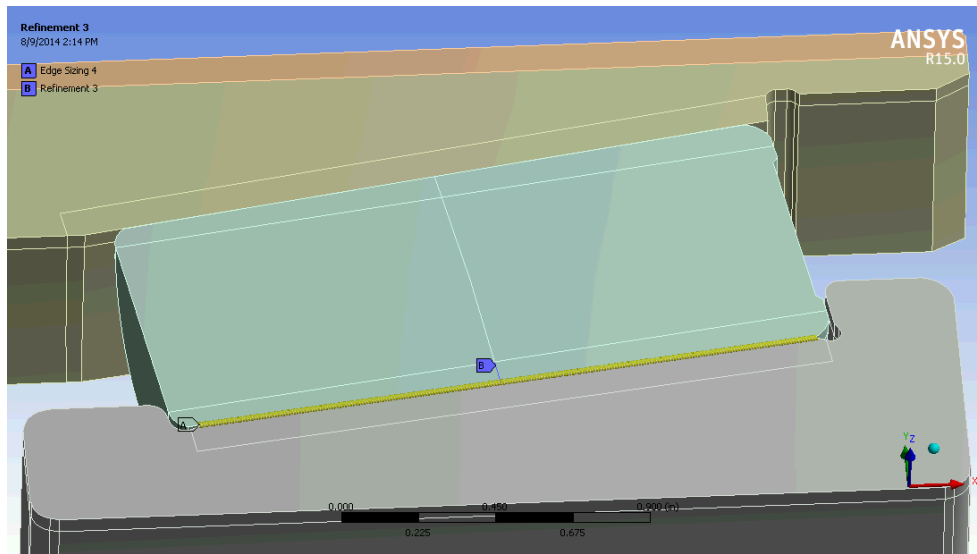
Figure 15: Mesh Refinement at the Center of the Contact and Edge Sizing in the Primary Finite Element Model

With regards to the loads and boundary conditions used in the model, frictionless supports were used along faces on the symmetrical plane of the model, through the center of the contacting bearing components. Frictionless supports were also applied to the end faces of the cone in order to simulate contact with mating bearing components as well as the surface on the center plane of the bearing cup, as shown in Figure 16. A fixed support was used to constrain the model at the inner diameter of the cone, as it is press fit onto the axle of the railcar, and a load was applied to the edge of the cup geometry as would ordinarily be distributed by a nominal AAR bearing adapter (Figure 16). It should be noted that the impact of the hoop stress produced in the cone due to the press fit with the axle was not included in this model or the theoretical predictions in Chapter 2; therefore, these stresses were assumed to be negligible.
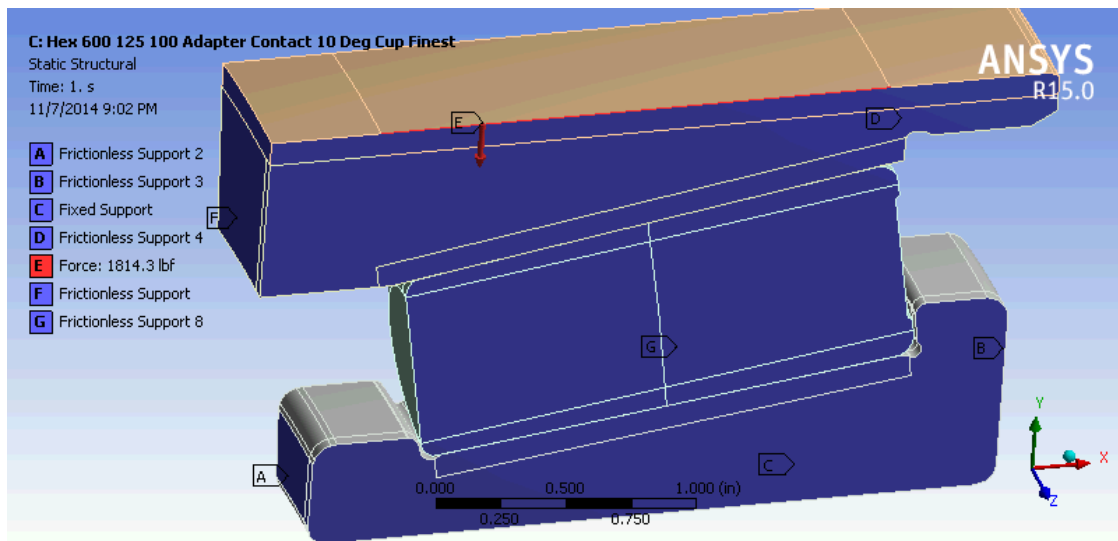
Figure 16: Load and Boundary Conditions in the Primary Finite Element Model

As indicated, the adapter load was assumed to be uniform across the outer diameter of the cup during this simulation (Figure 16). AAR adapters have two load pads, as shown in Figure 17, which mate with each raceway of the double row tapered roller bearing individually. Generally AAR adapters do an acceptable job of evenly distributing the load across both bearing raceways. However, as will be discussed in Chapter 4, under inordinate load conditions this is not always the case. Once validated, the finite element methods proposed could be used to study the impact of uneven adapter load distributions on the stress state inside the bearing.
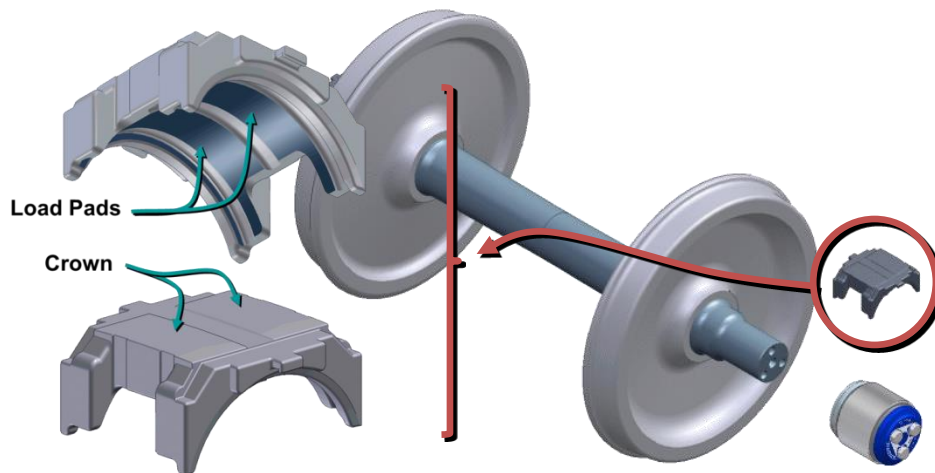
Figure 17: Association of American Railroads (AAR) Adapter Crown and Load Pads

An overview of finite element results will be discussed below and other settings used in the finite element model may be found in Appendix E. While Ansys Mechanical software was used to setup the model, a 64-bit Windows 2008 HPC server with 128 GB of RAM and 32 processers was used to compute finite element results using two Ansys HPC

software licenses. It should be noted that the computational limit of the server utilized for the analyses presented in this paper was reached and further investment in higher performance computing software or random access memory will allow for more detailed simulations in the future. Regardless of the computational limitations, the stress profile results achieved are indicative of those that would be expected under Hertzian contact conditions and are compared with theoretical results in detail in the next subchapter.

3.3 Primary Method for Hertzian Contact and Subsurface Stress Finite Element Modeling Results

To validate the accuracy of the proposed finite element method, initial finite element results will be compared with theoretical predictions intended for the identical contact geometry. It can be seen in Figure 18 that von Mises (Equivalent Stress) finite element results do not show any signs of edge loading as predicted by theoretical calculations related to the same geometry. Furthermore, an elliptical Hertzian contact stress profile is recognized in a cross section of the contact stress results (Figure 19) and when looking at the stress profile closely, it should be noted that the peak von Mises stress doesn't occur at the surface (Figure 20). This is the first indication that subsurface finite element stress predictions will match that of Figure 2.
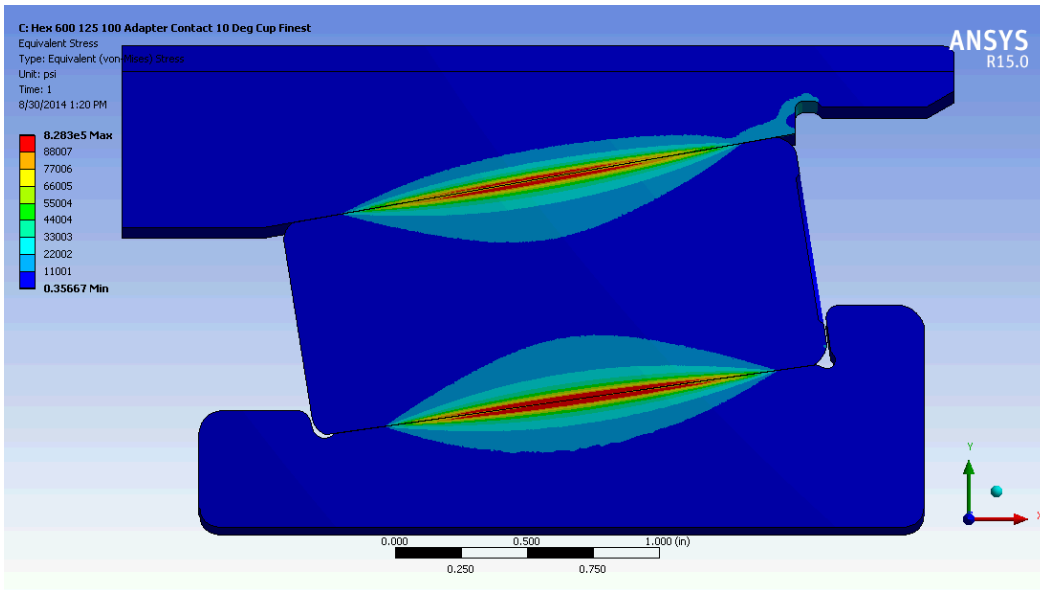
Figure 18: von Mises Contact Stress Results for Primary Finite Element Model
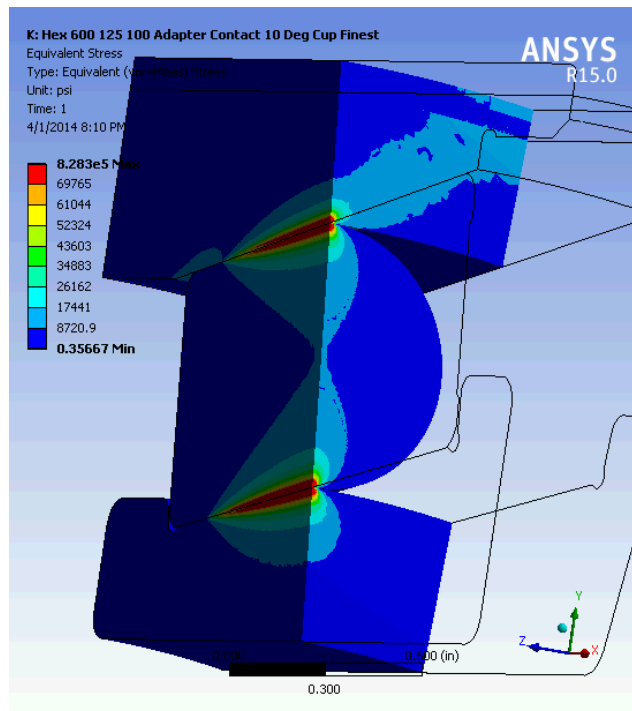
Figure 19: Cross Section of von Mises Contact Stress Results for Primary Finite Element Model through Midpoint of Roller

50
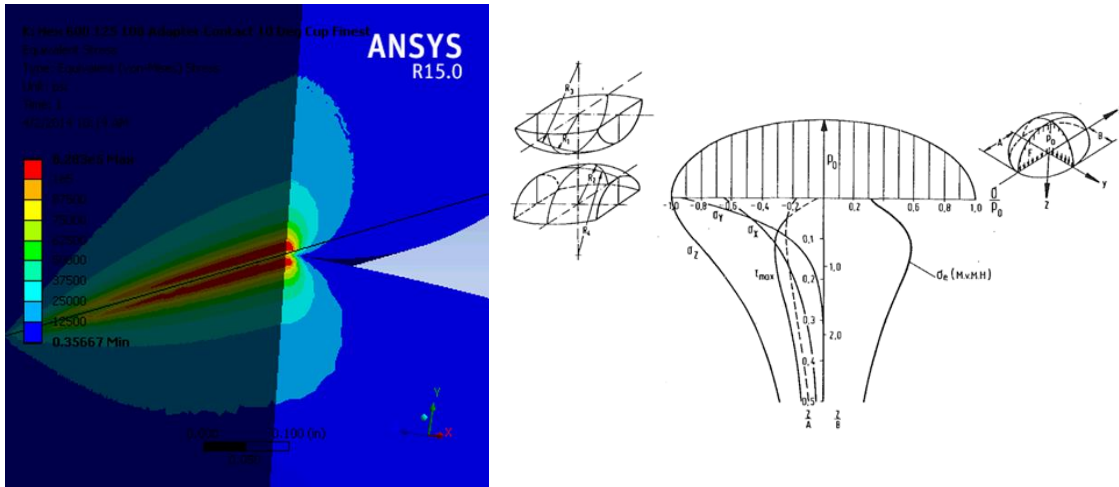
Figure 20: Cross Section of von Mises Contact Stress Results for Primary Finite Element Model through Midpoint of Roller at Inner Raceway

Accepting that the primary mode of stress under bearing loads is compressive in nature, minimum principle stress results are also of interest. It can be seen in Figure 21, that all of the bearing components are under compression as expected and an elliptical contact stress profile is again noted.
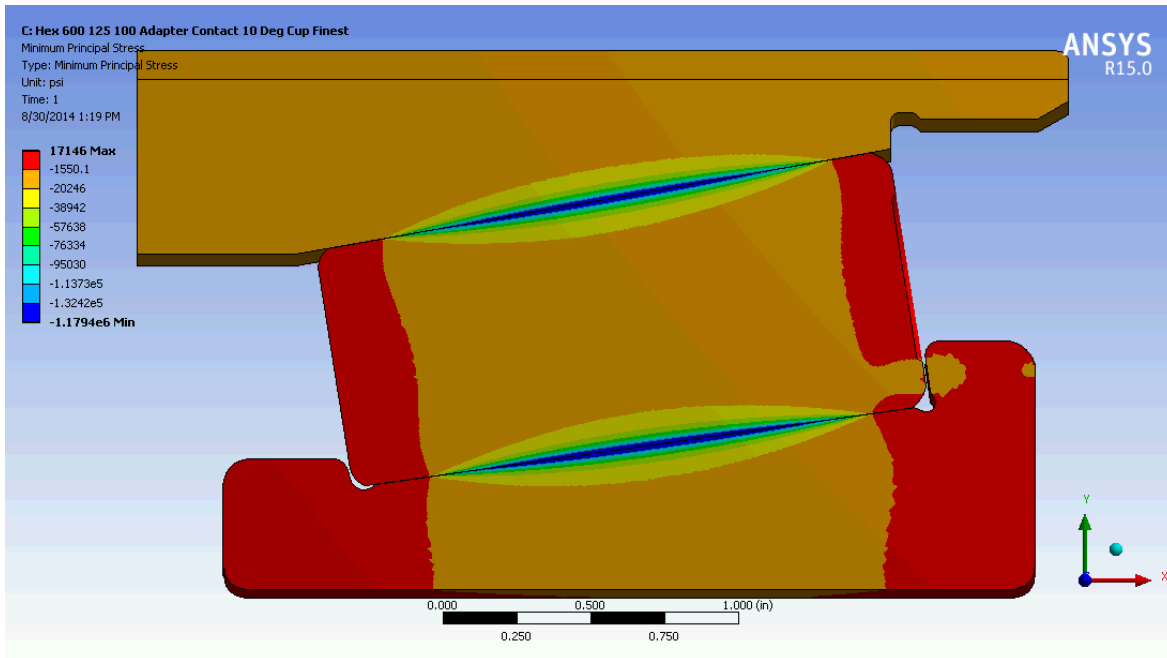
Figure 21: Minimum Principle Contact Stress Results for Primary Finite Element Model

As discussed in the introduction, Lundberg and Palmgren probability of survival relationships are still the bases of standard industry bearing life predictions. Maximum orthogonal shear stress results, as reflected on by Lundberg and found in equation (2), are shown in Figure 22 and Figure 23 for the primary simulation. It can be recognized when looking at these figures, that finite element analysis can be used to determine both the maximum orthogonal shear stress depth and magnitude. With further investment, it is possible that this type of simulation technology could be used to refine bearing life prediction tools for tapered roller bearings in the railroad industry.
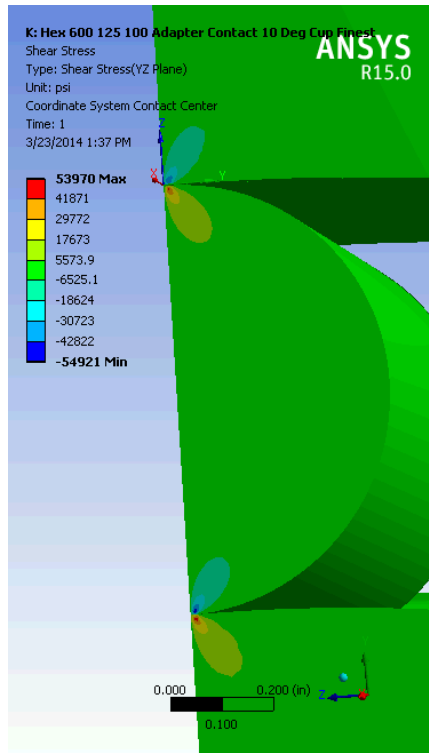
Figure 22: Orthogonal Shear Stress Results in both Inner and Outer Raceway for Primary Finite Element Model
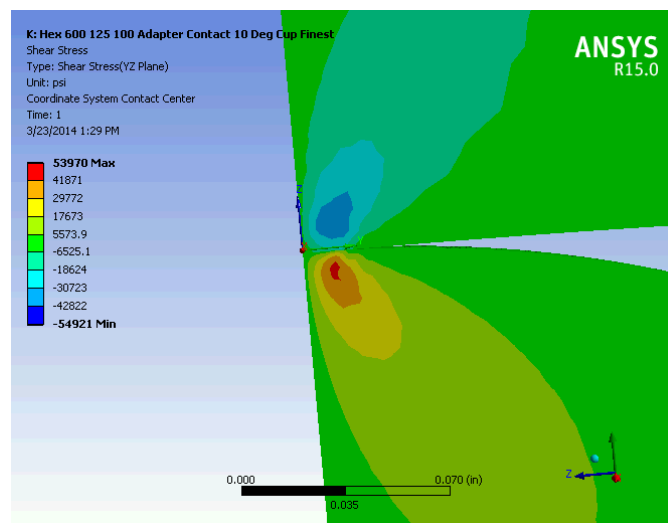
Figure 23: Orthogonal Shear Stress Results in Outer Raceway for Primary Finite Element Model

Numerical surface and subsurface stress values at the center of each contact region were also compared with theoretical predictions. The first comparison between contact pressure distributions at the surface of the components is shown below. The Hertzian contact pressure estimated along the semimajor axis of the contact ellipse between the roller and outer raceway may be seen in Figure 24. Meanwhile, the Hertzian contact pressure projected along the semimajor axis of the contact ellipse between the roller and inner raceway may be seen in Figure 26. When relating finite element and theoretical results, there is a 4.2% and 9.4% difference between finite element results and theoretical predictions for the inner and outer raceway maximum Hertzian contact pressure respectively. The greater difference between Hertzian predictions and finite element results for the pressure distribution between the roller and outer raceway is thought to be due to deflection of the outer raceway. As shown in Figure 12, the crown geometry of the roller and outer raceways were perfectly centered in relation to one another. Therefore, geometric alignment of the crown is an unlikely cause. When looking at the deflection of the cup in Figure 25, it can be seen that the flexible behavior of the cup may have an impact on the contact stress profile, as the component tends to slightly deflect around the roller under the adapter load. Although the magnitude of the deflection of the cup seen in Figure 25 is minimal, not much flexure is required to impact the contact geometry and resulting pressure distributions on precision ground bearing components. Hertzian theory assumes the force is completely perpendicular to the contact plane amid two elliptical bodies and does not account for bending of the elliptical surfaces in contact.

54
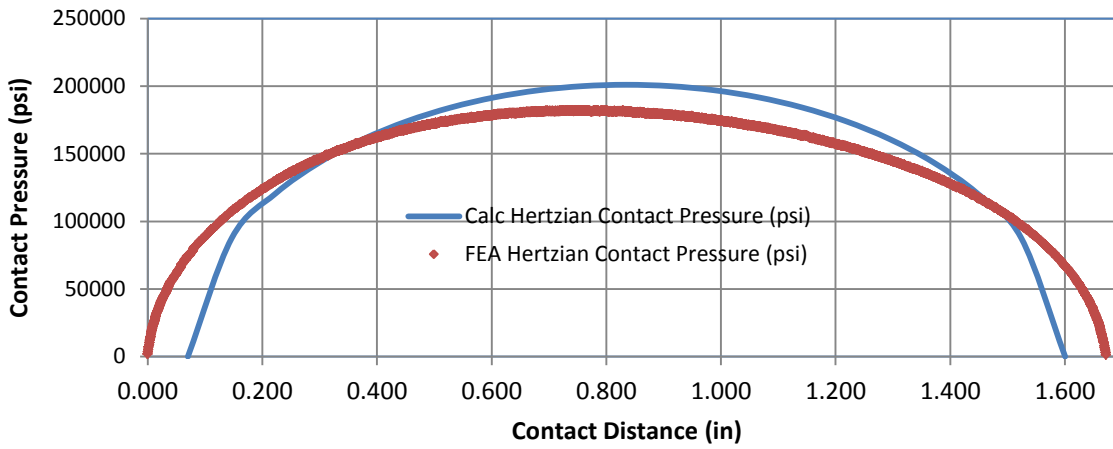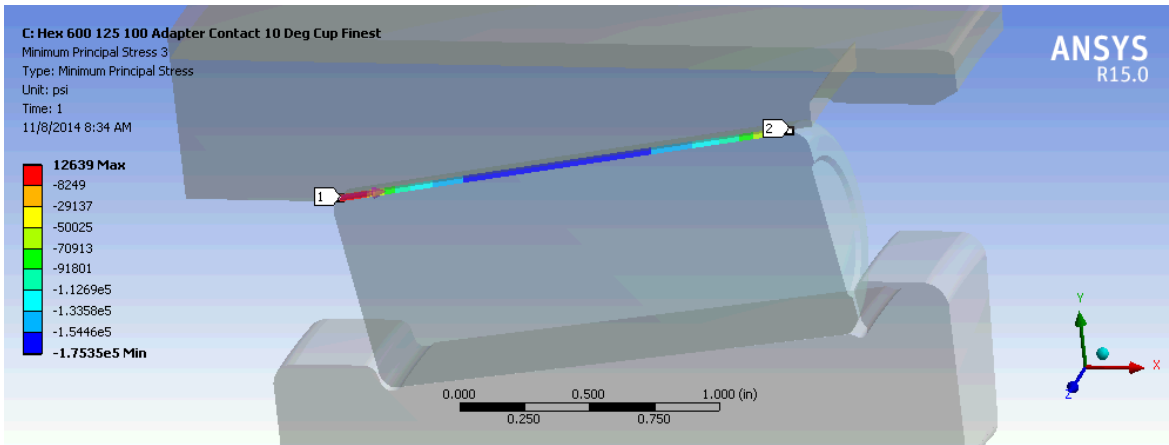
Figure 24: Hertzian Contact Pressure between Outer Raceway and Roller along the Semimajor Axis of the Hertzian Contact Ellipse during Primary Finite Element Analysis
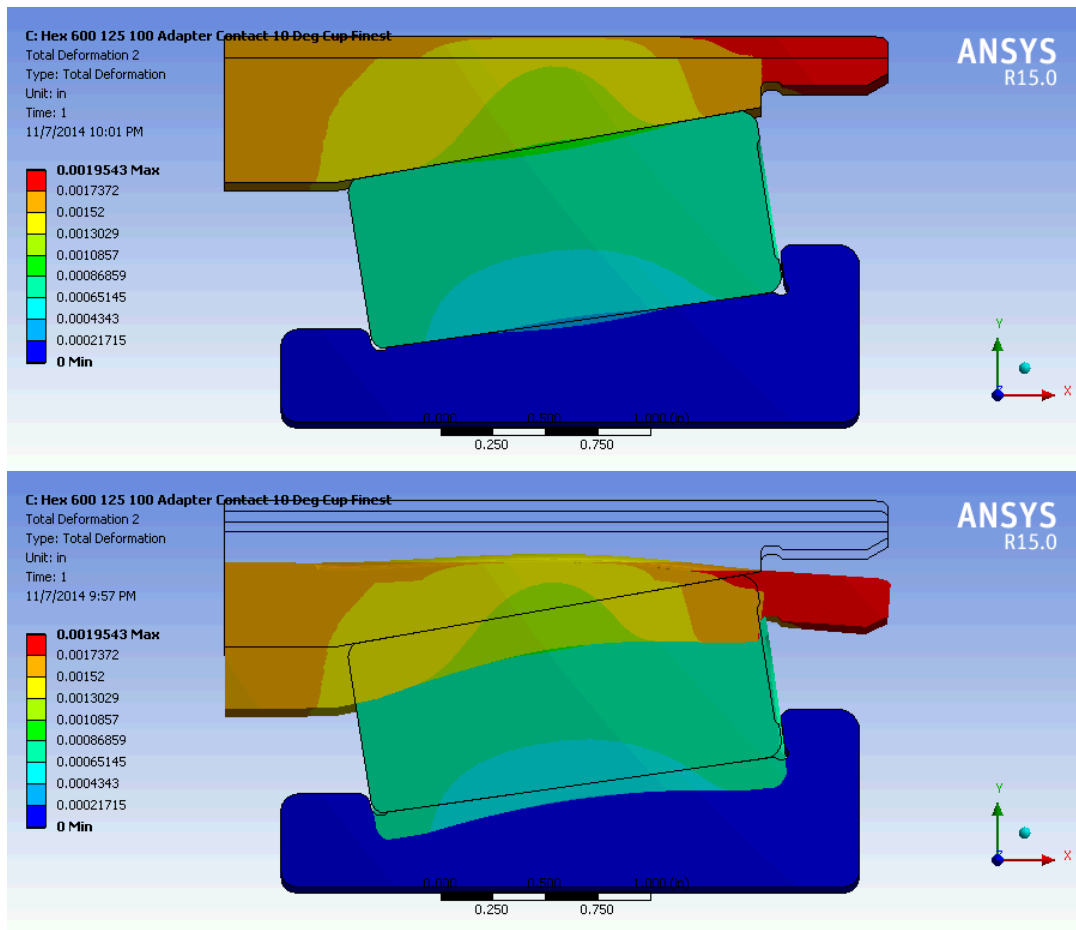
Figure 25: Deflection of Outer Raceway during Primary Finite Element Analysis with Full Scale Results (top) and 200x Scaled Results (bottom) for Enhanced Demonstration
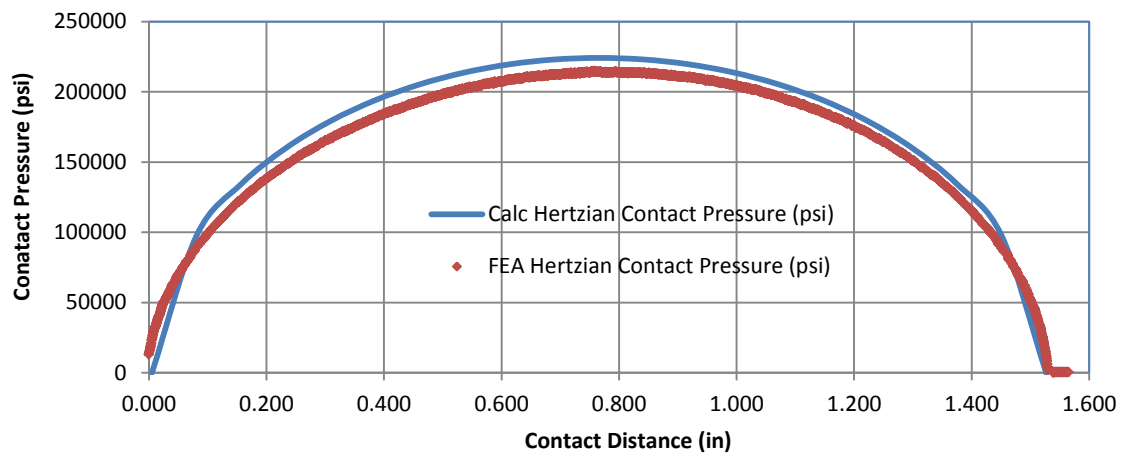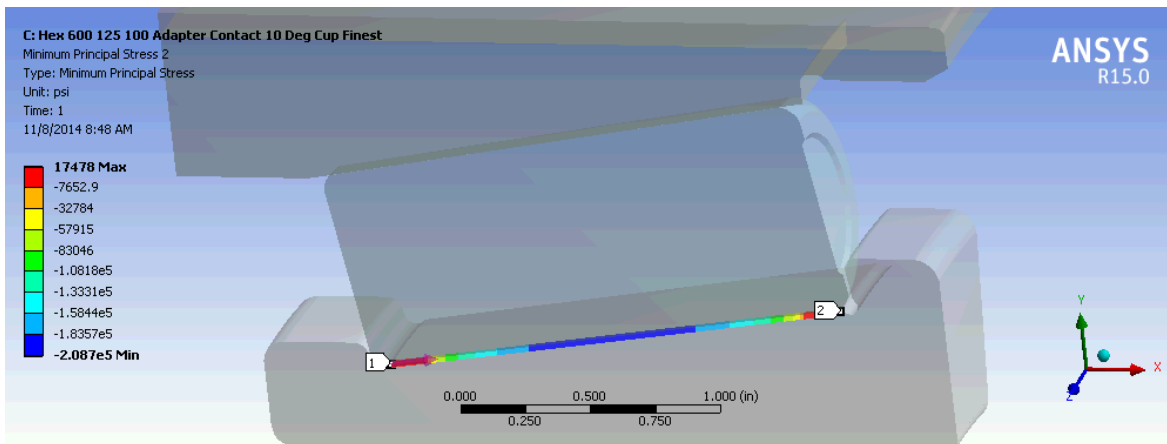
Figure 26: **Hertzian Contact Pressure between Inner Raceway and Roller along the Semimajor axis of the Hertzian Contact Ellipse during Primary Finite Element Analysis**

When comparing Hertzian contact pressure results along the semiminor axis of the contact ellipse, there is also a reasonably close correlation between finite element and bearing theory (Figure 27 and Figure 28). Nonetheless, when looking at the contact stress distribution along the semiminor axis, it can be seen that finite element results do not exhibit the exact same semiminor axis length as equation (24). This may be another reason for the slight difference in pressure maxima outcomes between established bearing theory

57

and finite element results. This semiminor axis length difference is believed to be due to more compliant deflection of the components in the model in order to mate with each other in contact than anticipated by Hertzian theory, which assumes infinite radii and normal loading without bending.
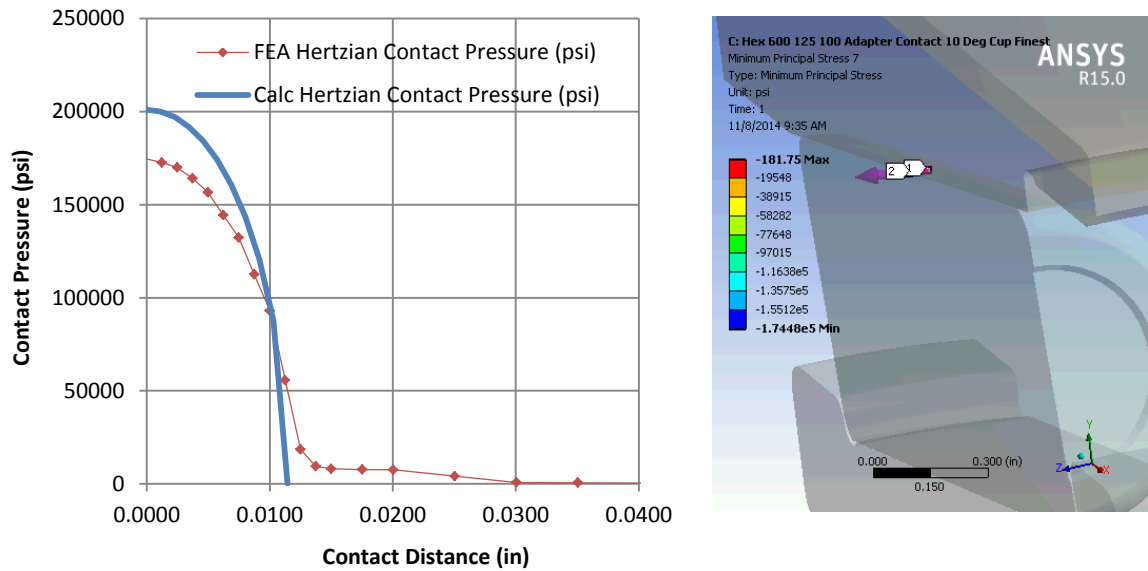
Figure 27: **Hertzian Contact Pressure between Outer Raceway and Roller along the Semiminor axis of the Hertzian Contact Ellipse during Primary Finite Element Analysis**
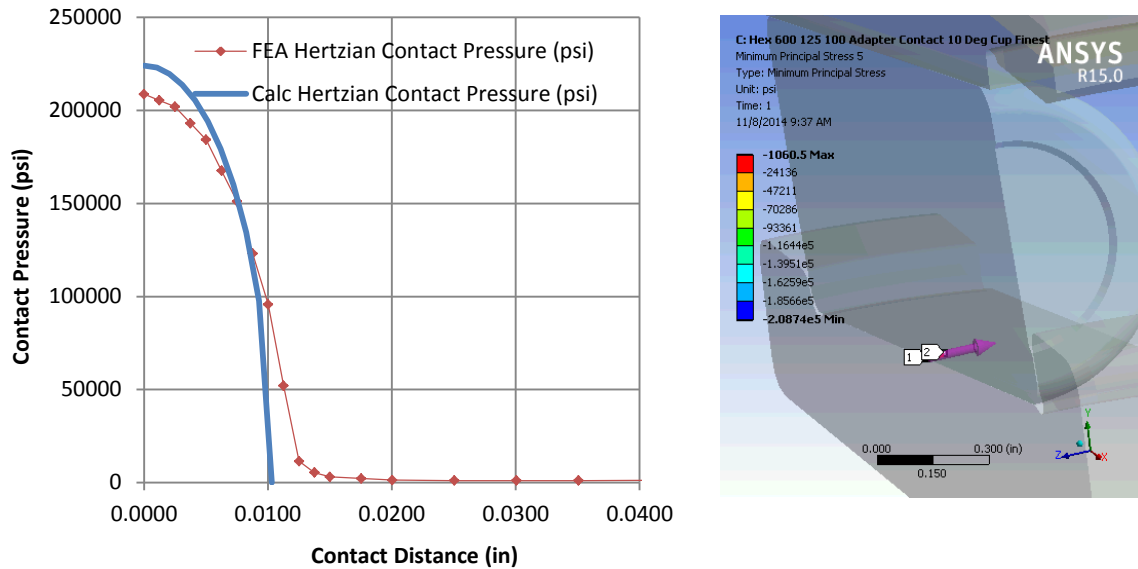
Figure 28: **Hertzian Contact Pressure between Inner Raceway and Roller along the Semiminor axis of the Hertzian Contact Ellipse during Primary Finite Element Analysis**

Subsurface stress distributions along the centerline of the roller crown may be seen in Figure 29 and Figure 30. Subsurface stress finite element results also match theoretical predictions very well. All magnitude and depth results corresponded within 10,000 psi and .001 inches correspondingly for the inner raceway contact while there was weaker correlation between theory and finite element results for the outer raceway contact. The greater deviation between peak surface pressure magnitude on the outer raceway than the inner raceway is noted in subsurface stress results as well. Further details associated with von Mises and maximum shear stress result correlations are shown in Table 1. Although there was very good agreement between theory and primary finite element results, other modeling options were investigated for lower computational expense and improved accuracy, which are discussed in the following subchapter.

Table 1: Correlation between Primary Finite Element Method and Theoretical Predictions, Peak Maximum Shear Stress and von Mises Stress, Magnitudes and Depths

Subsurface Stress Results for Inner Raceway Contact			
Ultimate Stress Parameter	**Finite Element**	**Bearing Theory**	**% Difference**
Maximum Shear Stress Peak Magnitude (psi)	62915	67905	7.35%
Maximum Shear Stress Depth (in)	0.008	0.008	0.00%
von Mises Stress Peak Magnitude (psi)	116460	126152	7.68%
von Mises Stress Depth (in)	0.008	0.007	12.50%
Subsurface Stress Results for Outer Raceway Contact			
Ultimate Stress Parameter	**Finite Element**	**Bearing Theory**	**% Difference**
Maximum Shear Stress Peak Magnitude (psi)	52697	61651	14.52%
Maximum Shear Stress Depth (in)	0.008	0.009	11.11%
von Mises Stress Peak Magnitude (psi)	98871	114504	13.65%
von Mises Stress Depth (in)	0.008	0.008	0.00%
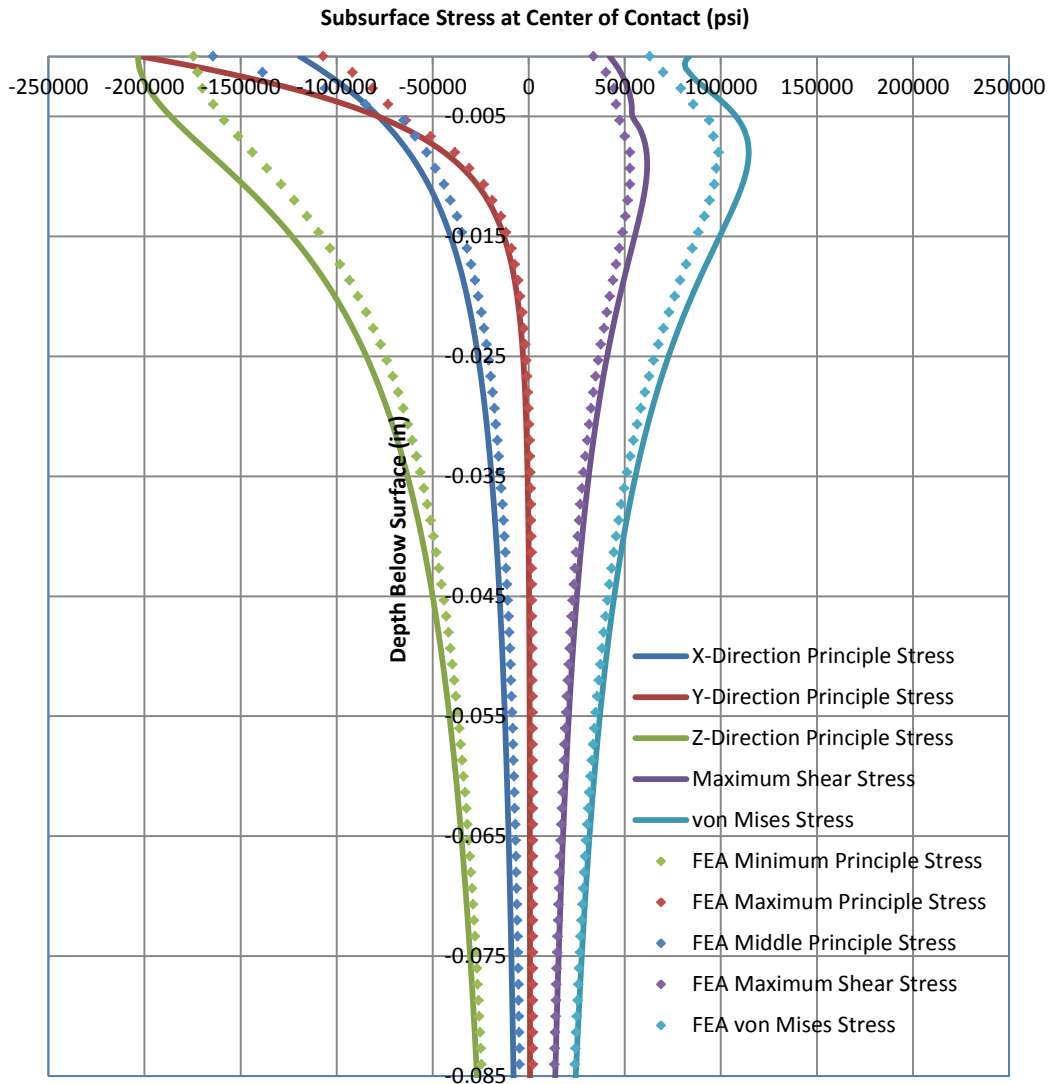
Figure 29: Subsurface Stress between Outer Raceway and Roller at Center of the Contact during Primary Finite Element Analysis

61

Figure 30: Subsurface Stress between Inner Raceway and Roller at Center of the Contact during Primary Finite Element Analysis

62
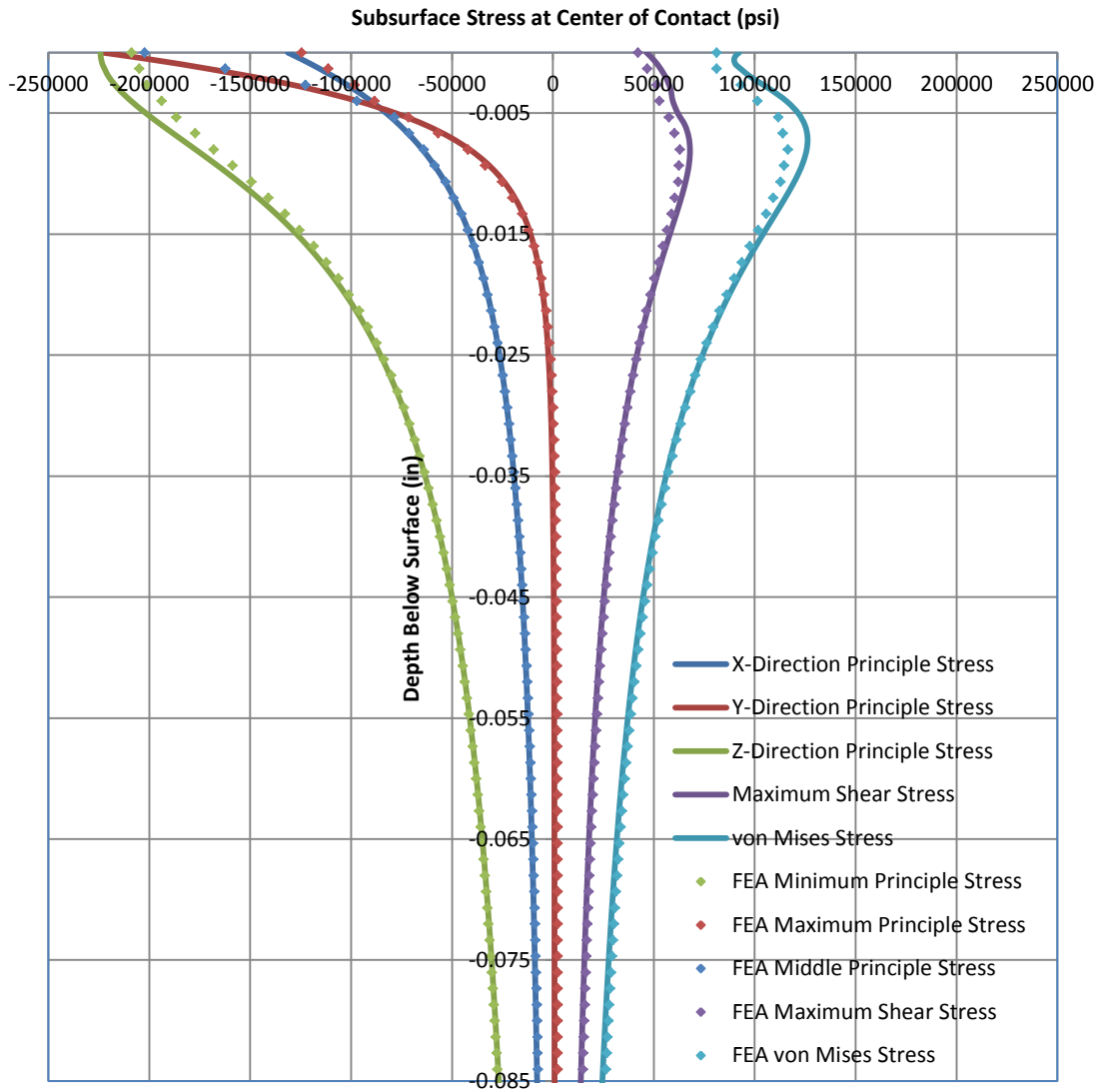
3.4 Second Method for Hertzian Contact and Subsurface Stress Finite Element Modeling, Including Back Rib Contact

When the roller was allowed to position itself in the finite element model without the adjust to touch setting on the roller interface treatment with the back rib of the cone, the roller crown was more focused on the inner raceway crown. This can be seen when comparing Figure 31 below with Figure 12 of the primary finite element simulation. This roller orientation was found to result in a slightly closer correlation between finite element and theoretical stress results for the inner raceway, as will be presented below. Meanwhile, the outer raceway was constrained slightly asymmetrically in order to determine what impact this would have on finite element results (Figure 31).
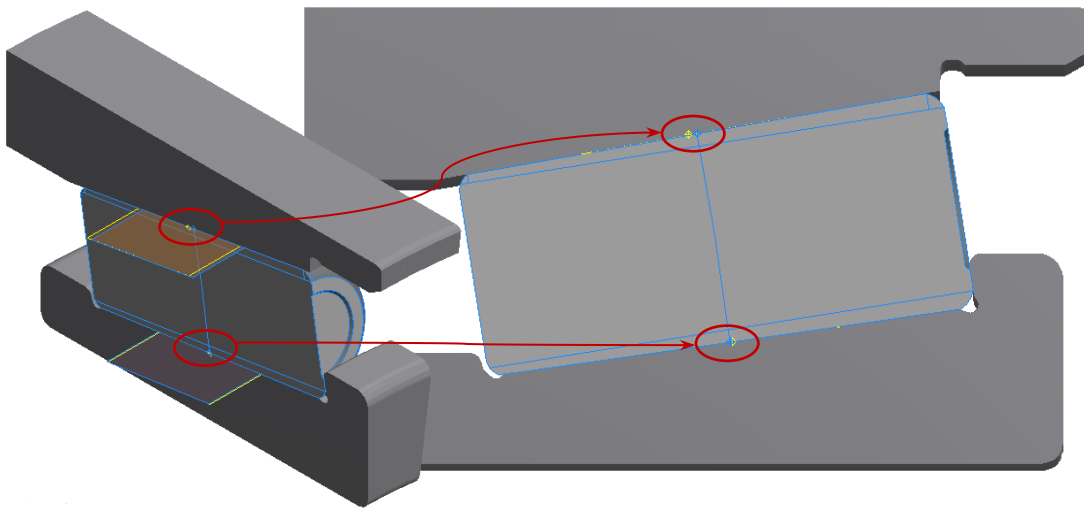
Figure 31: Lateral Position of Tapered Roller in between Inner and Outer Raceways with Roller Allowed to Contact the Back Rib of the Cone in Second Finite Element Model

63

The surfaces in the second simulation were partitioned differently than the first but many of the same mesh control and refinement methods were used. Some of the differences between the first and second mesh (Figure 32) include: increasing the contact relevance between the roller and the back rib of the cone to 75%, decreasing the size and refinement of the partitioned surfaces near the raceway contacts to a refinement level of two, decreasing edge sizing in the raceway contacts to .00175 inches, reducing the refinement of the central axis of the roller crown to one, and adding subsurface refinements near the edges of the raceway for post processing of subsurface stresses. This resulted in 14,489,151 nodes and 10,429,881 elements, which was slightly less computationally expensive than the primary finite element method. Meanwhile, all of the loads and boundary conditions used in the second model were identical to the first. Stabilization was also used on all of the contact regions in the model to help converge the model but the "adjust to touch" constraint between the back rib of the cone and the large end of the roller was no longer employed. This allowed for the contact forces and stresses created by roller contact with the back rib of the cone to be analyzed, as will be discussed in the next subchapter.
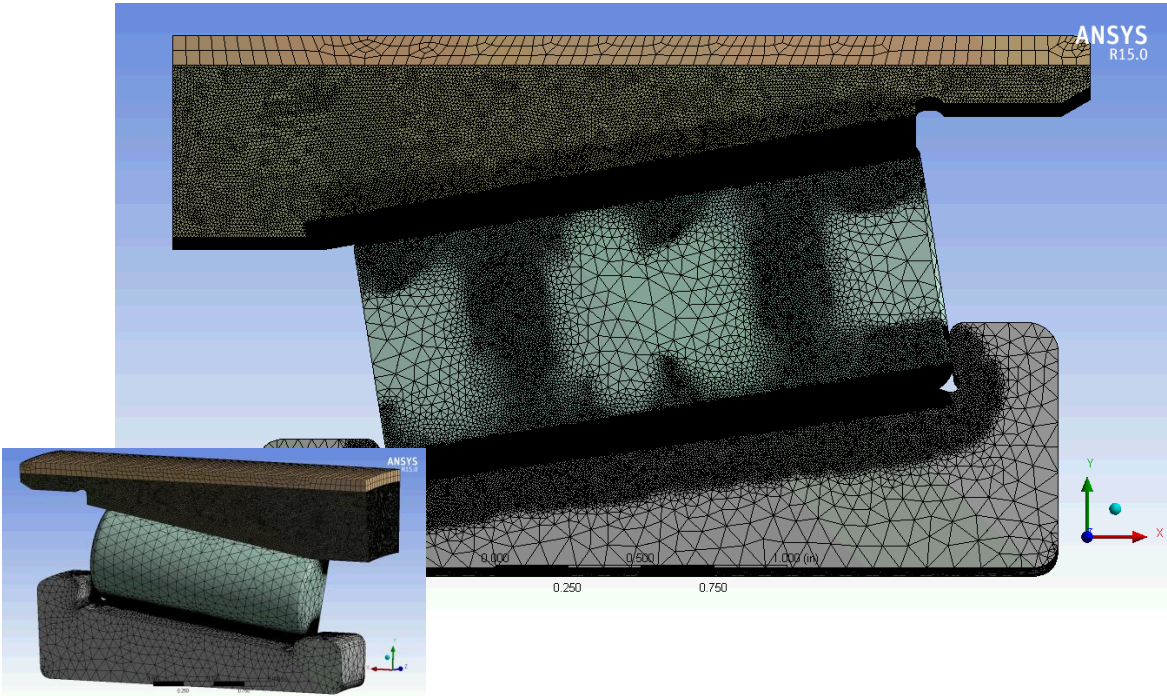
Figure 32: Mesh in Second Finite Element Model

3.4 Second Method for Hertzian Contact and Subsurface Stress Finite Element Modeling Results, Including Back Rib Contact

When the roller was allowed to position itself in the finite element model without the adjust to touch setting on the roller interface treatment with the back rib of the cone, a Hertzian point contact stress was created between the back rib of the cone and the large end of the roller, as displayed in Figure 33. The reaction force Q_f in this location is of interest and is shown in Figure 34. After studying the components of the force in Figure 34, it was discovered that the angle of the reaction force θ_f was in between that of θ_i and the average of the inner and outer raceway angles $\frac{\theta_o + \theta_i}{2}$. However, it was much closer to θ_i than $\frac{\theta_o + \theta_i}{2}$ and the magnitude was within 0.11% of the reaction force calculated using equation (48) for the bearing design modeled. Given that θ_f is nearly equivalent to θ_i, equation (47) predicts that the reaction force seen by the roller from the inner raceway will not exactly equal that of the outer raceway. This is supported by the finite element results from the second finite element analysis presented in Table 2 as a percentage of the applied Stribeck load Q_{max}.

Table 2: Forces inside the Bearing as a Percentage of the Applied Stribeck Roller Load

Force between Bearing Components	% of Stribeck Roller Load
Force between Outer Raceway and Roller Outer Diameter	101.57%
Force between Inner Raceway and Roller Outer Diameter	101.53%
Force between Roller End Face and Back Rib of Cone	3.37%
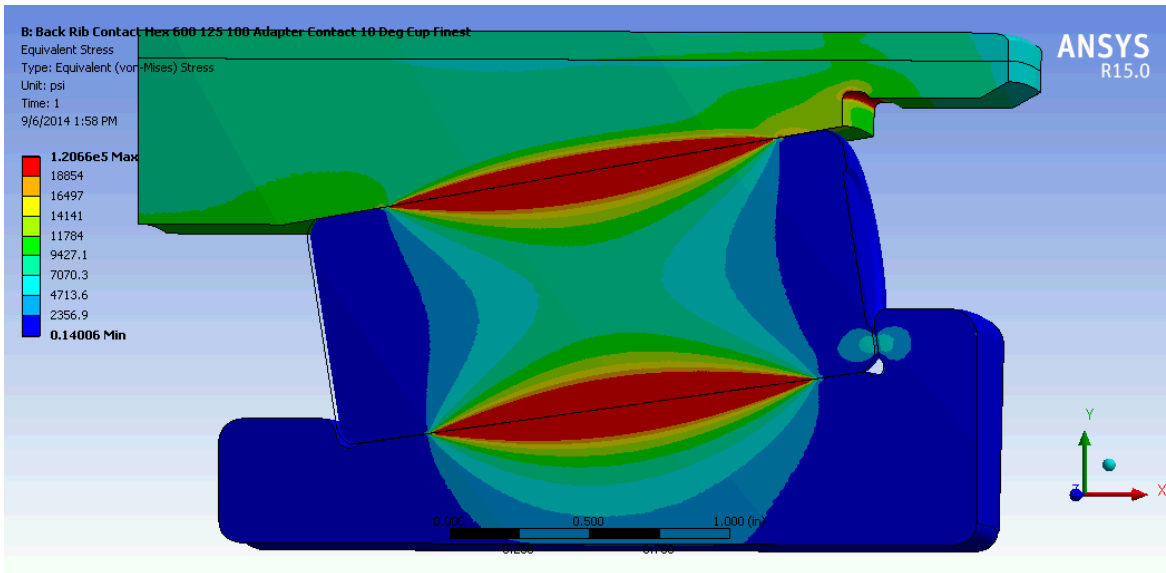
Figure 33: Equivalent Stress Profile on Roller Including Cone Back Rib Contact in Second Finite Element Model
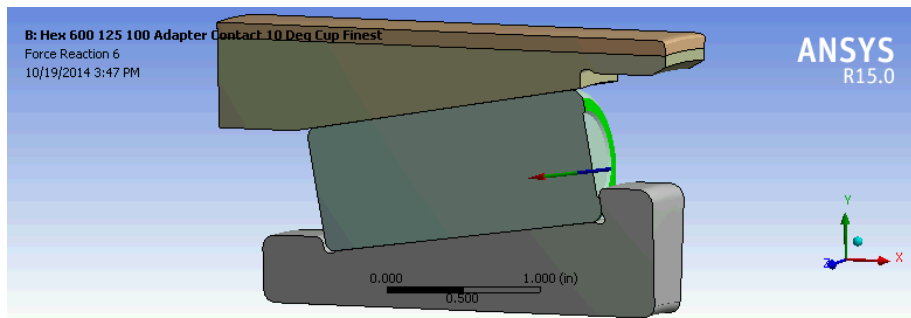
Figure 34: Reaction Force Q_f on the Back Rib of the Cone from Second Finite Element Model

Misalignment between the central axis of the roller crown and the central axis of the outer raceway crown might have some influence on minimum principle stress results at the surface (Figure 31). However, compared to the impact of outer raceway deflection, misalignment of crown geometry appears to be negligible when relating Figure 35 to

Figure 24. Meanwhile the alignment between the roller and the cone crown was enhanced during the second simulation, as compared to the primary simulation in Figure 31, which resulted in even better correlation between theoretical and finite element results as displayed in Figure 36.
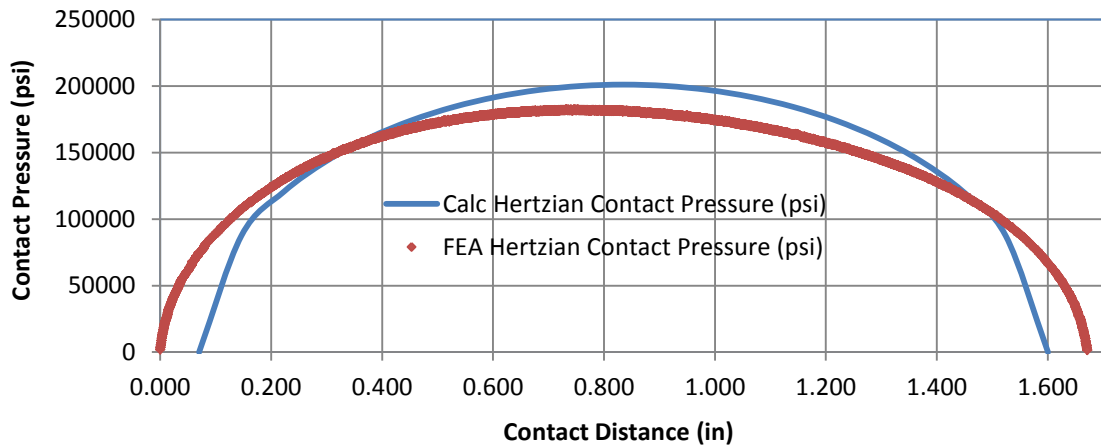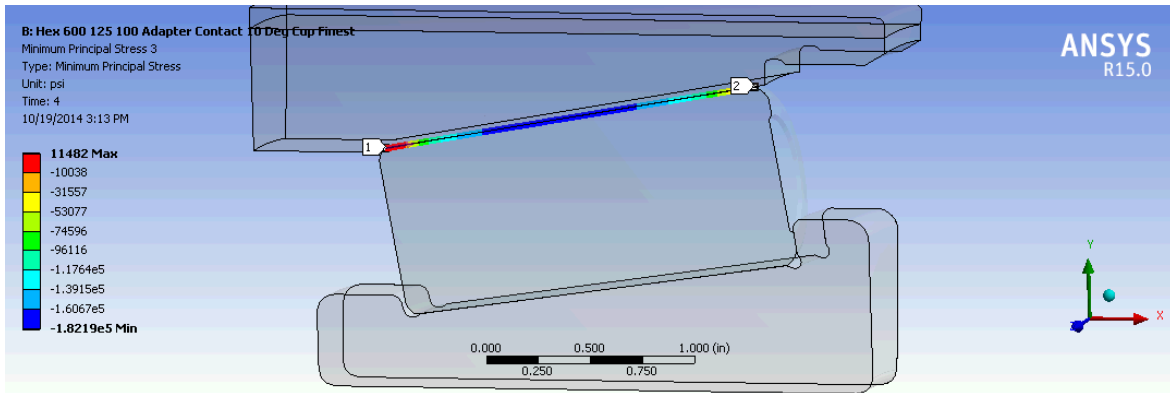
Figure 35: Hertzian Contact Pressure between Outer Raceway and Roller along the Semimajor axis of the Hertzian Contact Ellipse for Second Analysis with Back Rib Contact
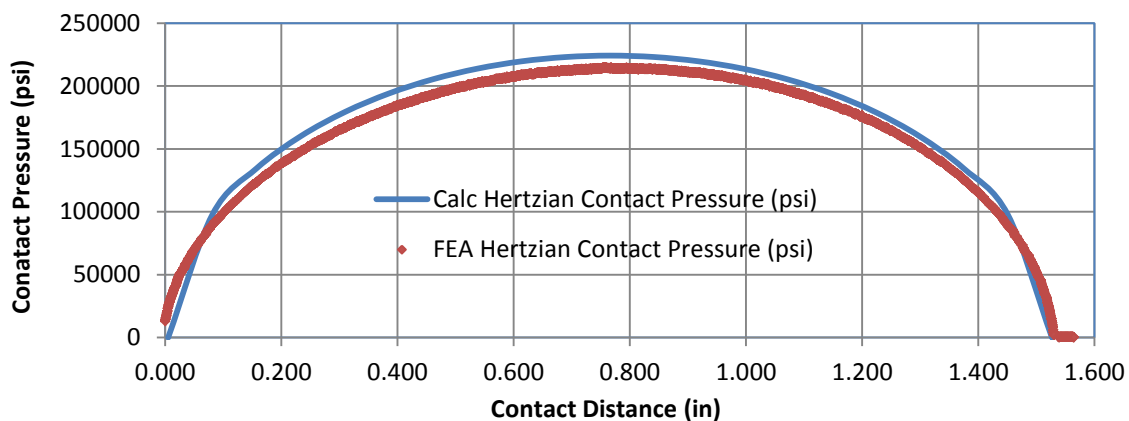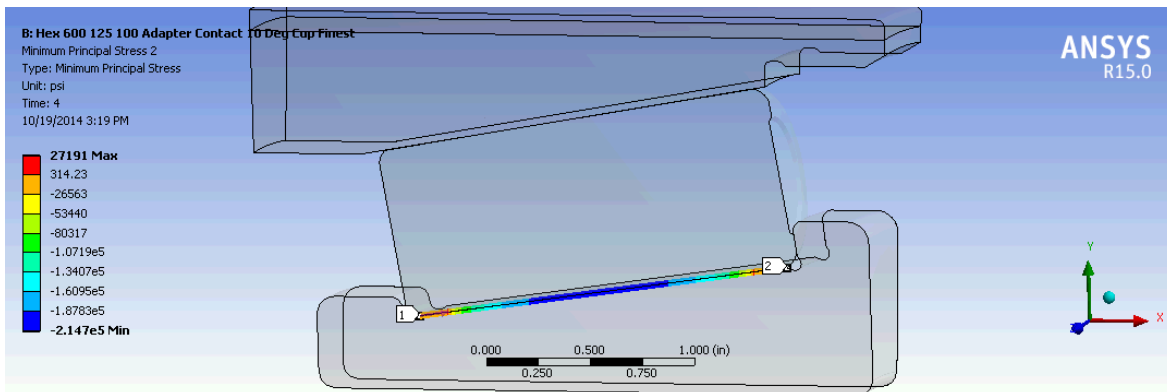
Figure 36: **Hertzian Contact Pressure between Inner Raceway and Roller along the Semimajor axis of the Hertzian Contact Ellipse for Second Analysis with Back Rib Contact**

With improved alignment of the crown geometry, the subsurface stresses created by roller contact with the inner raceway are illustrated in Figure 37. This demonstrates that the influence of the back rib of the cone contact with the roller end appears to be insignificant when analyzing raceway subsurface stresses under frictionless contact. Also, subsurface stress results from the improved inner raceway alignment are compared with primary finite element results in Table 3. It can be seen that the second finite element method results in better correlation between Hertzian theory and finite element methods.

69

Conversely, as mentioned in the introduction, roller skewing can aggravate the stress state in the bearing. Predominantly with frictional contact, as experienced in actual bearing applications, the influence of the back rib contact on the roller with regards to roller skewing is still an important consideration when making bearing design improvements.
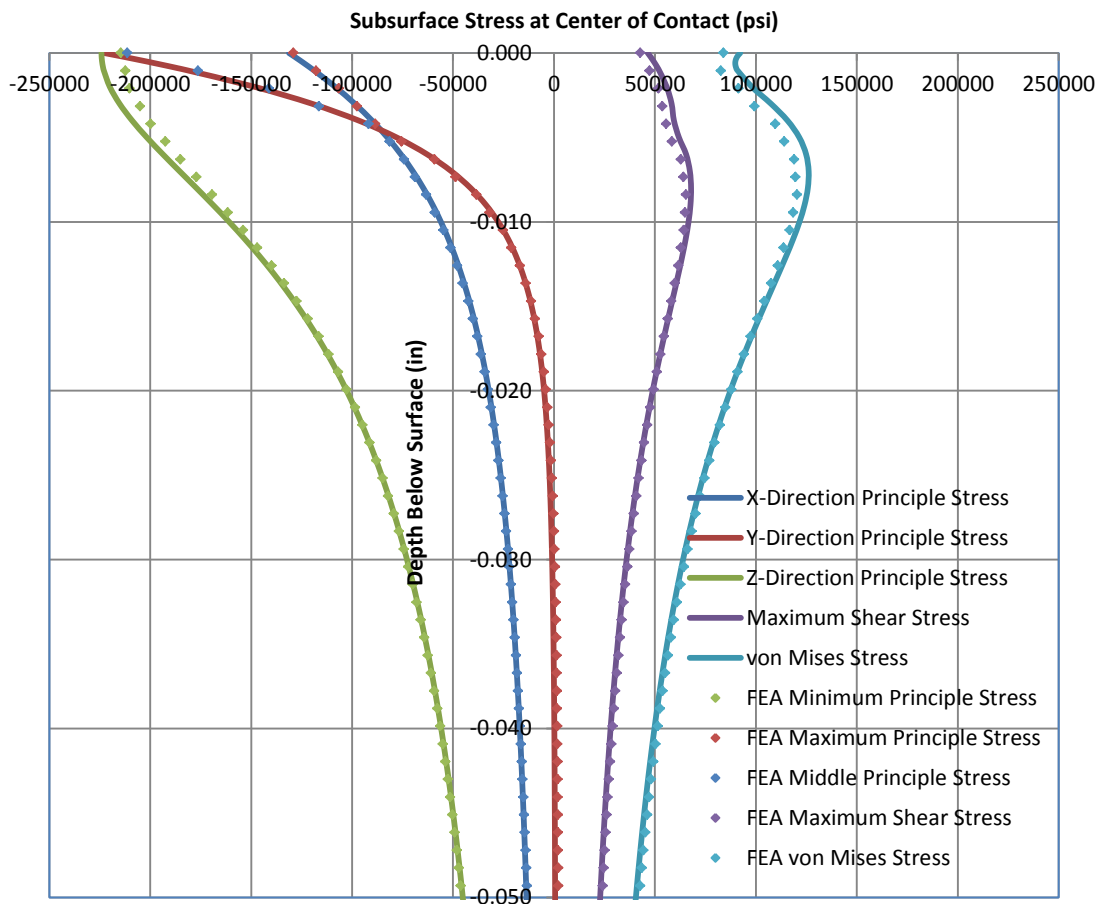
Figure 37: Subsurface Stress between Inner Raceway and Roller at the Center of the Contact during the Second Finite Element Analysis with Back Rib Contact Included

Table 3: Correlation between Finite Element Predictions of Peak Maximum Shear Stress and von Mises Stress, Magnitudes and Depths, for Primary and Second Finite Element Methods

Subsurface Stress Results for Inner Raceway Contact using Primary Finite Element Method			
Ultimate Stress Parameter	**Finite Element**	**Bearing Theory**	**% Difference**
Maximum Shear Stress Peak Magnitude (psi)	62,915	67,905	7.35%
Maximum Shear Stress Depth (in)	0.008	0.008	0.00%
von Mises Stress Peak Magnitude (psi)	116,460	126,152	7.68%
von Mises Stress Depth (in)	0.008	0.007	12.50%
Subsurface Stress Results for Inner Raceway Contact using Second Finite Element Method			
Ultimate Stress Parameter	**Finite Element**	**Bearing Theory**	**% Difference**
Maximum Shear Stress Peak Magnitude (psi)	65477	67,905	3.58%
Maximum Shear Stress Depth (in)	0.008	0.008	0.00%
von Mises Stress Peak Magnitude (psi)	120450	12,615	4.52%
von Mises Stress Depth (in)	0.008	0.007	12.50%

4. Demonstration of Practical Application of the Finite Element Analysis Tool, Discussion of Benefits, and Future Work

Based on the results of the two finite element analyses presented in Chapter 3, it is obvious that the proposed modeling methodology can accurately predict surface and subsurface bearing contact stresses. To demonstrate the benefits of the novel modeling methodology developed, some different load scenarios and contact geometries are discussed in Chapter 4, including those that may result from defective applications. Additionally, several areas for future work related to surface stress and fatigue life prediction of tapered roller bearings utilized in the railroad environment are proposed.

4.1 Bogie Systems and Load Conditions in the Railroad Environment

Tapered roller bearings for railcar applications are precision ground to extremely tight tolerances in comparison to the bogie assemblies and railcars that they are designed to carry. Bearing adapters or housings are machined to mate with the outer raceway of the bearing in most applications. The majority of bearing adapters used in freight cars are cast with crowned surfaces to evenly distribute the load from the railcar onto the outer raceway of the bearing (Figure 17).   Although the adapter crown is designed to compensate for some misalignment, either poor bogie design or quality can still have a negative impact on bearing life. Bearing designers in the railroad industry are commonly asked to conduct bearing failure analyses on failed bearings in order to determine the root cause of the failure. This is due to the fact that many of the bogie performance issues seen in service can be identified through an assessment of bearing condition. Some of the most frequent bogie system issues discovered are related to: adapter machining, pedestal roof flatness, spring group assembly, side frame variation, bogie shift, and bogie warp.

Alternatively, wheel set issues can also have a detrimental impact on the stress state and resulting life of the bearing. Wheel fatigue resulting in shelling and wheel flats, classically caused by railcar breaking system issues, will frequently give rise to impact loads that will result in brinelling of bearing raceways. Brinelling defects are currently allowed to return to service, according to current AAR reconditioning standards [15]. It has been noted that brinelling defects will often result in fatigue spalling, which is evident

by the shape of the spall pattern that occurs in the raceway. A specific spall pattern occurs due to the stress concentrations that surround the brinelled surface (Figure 38). In addition to the wheel, the quality of the axle is critical to the performance of the bearing, as even slight variations in journal diameter or cap screw hole thread condition can result in a loss of lateral bearing clamp which can also lead to fatigue spalling of raceway components. Additionally, as previously mention in the Introduction, common rail bearing reconditioning standards allow for the repair of spalls by grinding the spalled surface out of the raceway. This practice will commonly result in fatigue spalling around the repair due to the stress risers it creates at the surface. In summary, although all of the common bogie system issues cannot be covered, it can be seen that advanced bearing stress analysis techniques will not only be advantageous in the optimization of bearing designs, but also in the failure analysis of bogie system issues. Bearing modeling can be used to simulate aggressive load conditions and determine if any potential bearing failure modes may result from particular bogie issues. Some examples of common fatigue spalling patterns, that are seen as a result of bogie system issues, are shown in Figure 38.
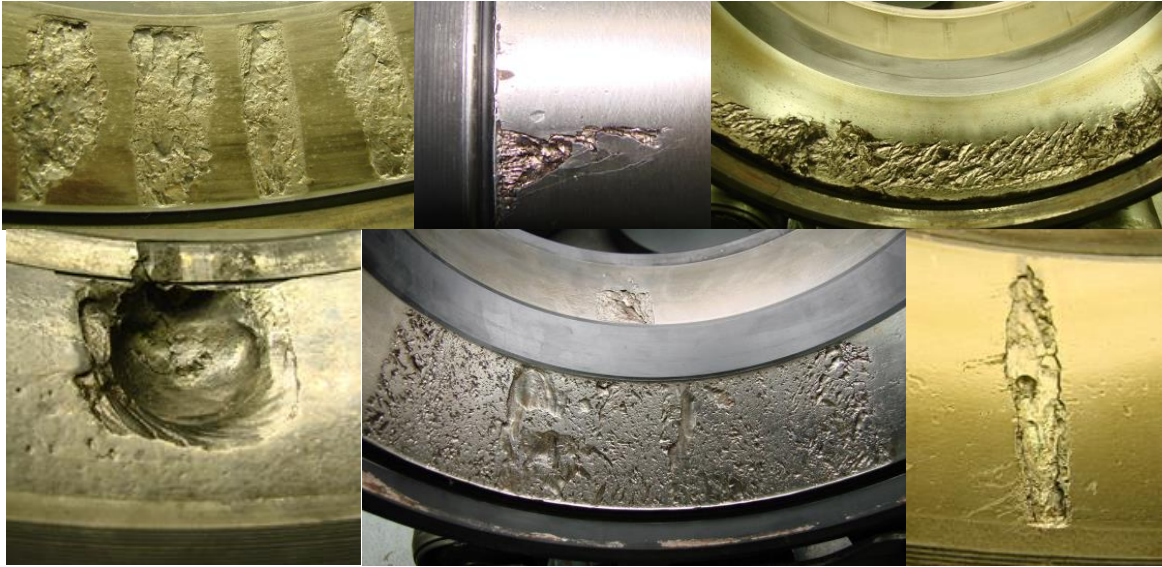
Figure 38: Rail Tapered Roller Bearing Fatigue Spalling Patterns due to a Bogie System Issues; Spalling due to Brinelling (top left), Load Distribution Issue Spalling (top center and top right), Adapter Issue Spalling (bottom left), Bogie Issue Spalling (bottom center), and Repaired Spall Spalling Propagation (bottom right)

Although some experts in the industry are able to ascertain the root cause of the failure, based on the damage pattern; it will be helpful to have confidence in advanced modeling tools. These tools can be employed to help predict the degree of misalignment, magnitude of load, and displacement of mating components required to cause specific types of bearing failures. Common bearing design theory, including Hertzian contact stress and Stribeck load distribution methods are not capable of providing answers. The accomplishment of developing a finite element tool that can accurately predict subsurface stresses associated with edge and lateral loading will be very helpful to railroad bearing designers.

As presented in the introduction, in order to reduce cost and simplify bogie assemblies, railcar designers often apply the same bearing design to multiple railcar

designs with varying load ratings. The goal of reducing cost and simplifying bearing supply is well warranted; however, this presents bearing designers with the additional challenge of optimizing these designs to perform adequately in all applications. Bearing designers may also choose to consider imperfect railcar overloading conditions when working on detailed designs which will be discussed in more detail in the next subchapter.

4.2 Analysis of Contact Stress Under Severe Load Conditions

In the finite element simulations presented in Chapter 3, edge loading was avoided to allow for direct correlation with Hertzian contact theory. As previously discussed, commonly in the tapered roller bearing industry, bearing designs with modified line contacts are used to attain maximum utilization of the whole length of the raceway. Furthermore, railroad bearings often experience aggravated load conditions due to application issues, such as the bogie performance issues already conferred. These types of problems often result in edge loading of raceway components and can be identified by uneven fatigue between inboard and outboard cup raceways (Figure 38). Knowledgeable industry experts may recognize uneven wear on the adapter crown or outer diameter of the cup, displayed in Figure 39, as external evidence of this condition. In order to demonstrate the ability of the finite element tool developed to study the surface stresses on a raceway under edge load conditions, the Stribeck load in the model considered during the second finite element analysis was increased by 200% and 400% of the initial value. Equivalent stress results for each load scenario are compared in Figure 40. When looking specifically at the surface stress along the semimajor axis of the ellipse, it was discovered that surface stresses in the middle of the Hertzian contact region still adhered to Hertzian contact predictions while the stresses near the edge of the contact deviated from Hertzian theory (Figure 41). This would suggest that Hertzian theory, without the use of finite element analysis, can still be used to predict stress magnitudes and locations necessary for the

selection of material and heat treat specifications for given bearing geometries with

modified line contact, as long as severe edge loading is not present.

Figure 39: Indications of Uneven Loading in the Wear Patterns on the Adapter Crown and the Outer Diameter of a Cup
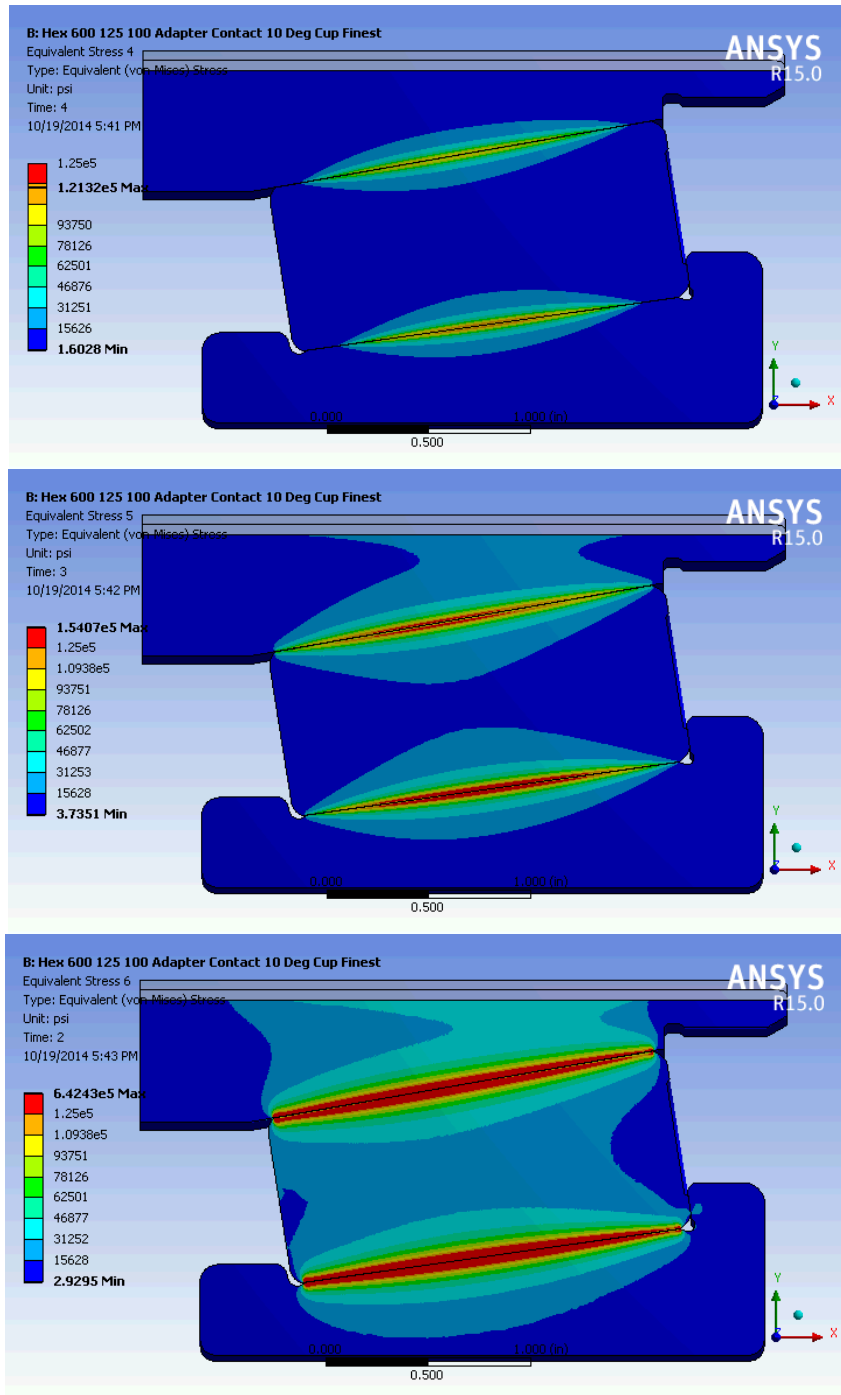
Figure 40: Comparison of Equivalent Stress Results for the Second Finite Element Model under Different Magnitudes of Adapter Load as follows: the Base Load (top), 200% of the Base Load (middle), and 400% of the Base Load (bottom)
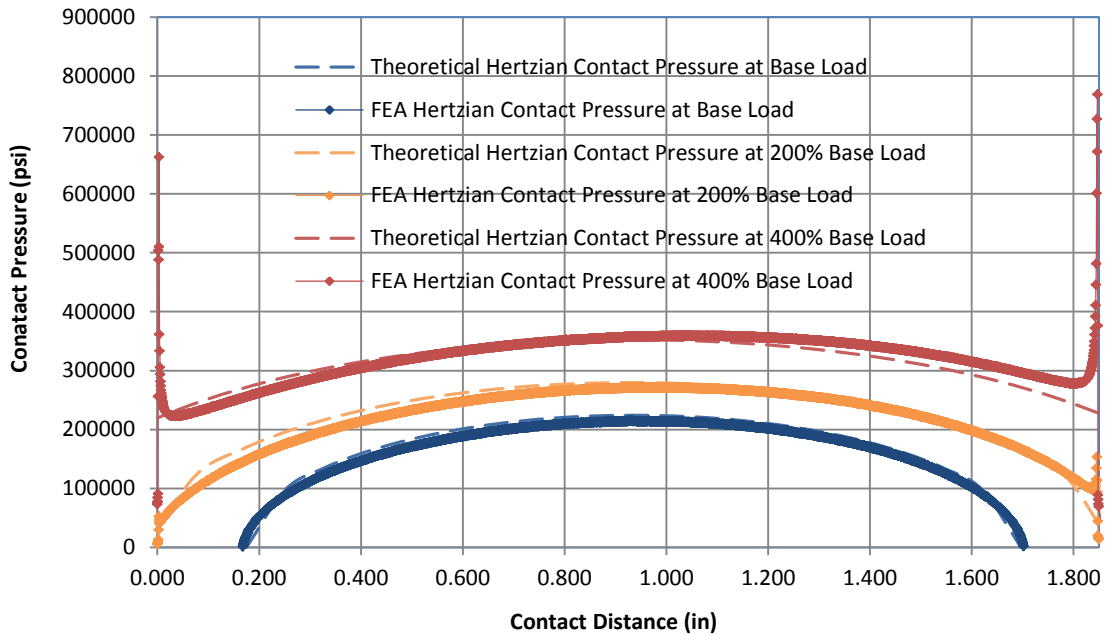
Figure 41: Hertzian Contact Pressure between Inner Raceway and Roller along the Semimajor axis of the Hertzian Contact Ellipse under Various Loads (Distance along the Roller Surface Starting from the Large End (LE) on the Left at 0.000 inches)

In reference to Figure 41, the potential for skewed contact stress profiles due to the misalignment of the roller and raceway crowns, as discussed in Chapter 3, might be recognized at each load condition. Alternatively, the effect of tapered roller geometry on Hertzian contact pressure results is more likely the cause for skewing of the contact pressure distribution. When comparing contact pressure results at each load, it should be noted that the orientation of the skewed profile can be used to predict which end of the roller or raceway will experience the most severe edge loading when it occurs. For example, the edge of the contact region with a contact pressure lower than that predicted for a perfectly concentric contact between two elliptical bodies under the base adapter load in Figure 41 appears to have less severe edge loading when the adapter load is increased by

80

400%. The bearing assessment benefits of the finite element tool developed should prove very powerful to rail bearing designers when studying the impact of alignment adjustments within the bearing, the influence of taper on railroad bearing designs, and detailed design modifications related to the prevention of edge load failure.

As mentioned, changes in the stress state below the surface due to variations in adapter load may also be studied using the finite element methodology developed. Demonstrated in Figure 42, the changes to the subsurface stress magnitude and depth due to increases in load may be analyzed. When looking at subsurface stress results at the center of the contact, it is interesting that the depth below the surface of the greatest maximum shear stress and von Mises stress magnitudes do not seem to change much even with a 400% increase in load. Additionally, subsurface finite element stress results still correlate well with Hertzian contact theory, even with the severe edge loading exemplified in Figure 41.

Subsurface Stress at Center of Contact (psi)

Legend:
- X-Direction Principle Stress
- Y-Direction Principle Stress
- Z-Direction Principle Stress
- Maximum Shear Stress
- von Mises Stress
- FEA Minimum Principle Stress
- FEA Maximum Principle Stress
- FEA Middle Principle Stress
- FEA Maximum Shear Stress
- FEA von Mises Stress
- X-Direction Principle Stress at Base Load
- Y-Direction Principle Stress at Base Load
- Z-Direction Principle Stress at Base Load
- Maximum Shear Stress at Base Load
- von Mises Stress at Base Load

Y-axis: Depth Below Surface (in)

Figure 42: Subsurface Stress between Inner Raceway and Roller at Center of the Contact at Base Adapter Load and 400% of Base Adapter Load

Finite element may also be used to analyze subsurface stress behavior at the edges of the raceway under distressed applications. This is exemplified in Figure 43, where subsurface stress results at both the large end (LE) and small end (SE) of the raceway are compared with subsurface stresses at the center of the raceway. It is fascinating to note that, although the magnitude of each stress increases, the location of the peak stress moves toward the surface of the component rather than away from it. This is similar to the stress

behavior experienced during lubricant breakdown or starvation, as evaluated by Broszeit [22,24] and Harris [8] by superposition of frictional shear stresses and Hertzian stresses. Even though all of the contacts included in the finite element simulations presented were frictionless, edge loading conditions still drive stress maxima to the surface.
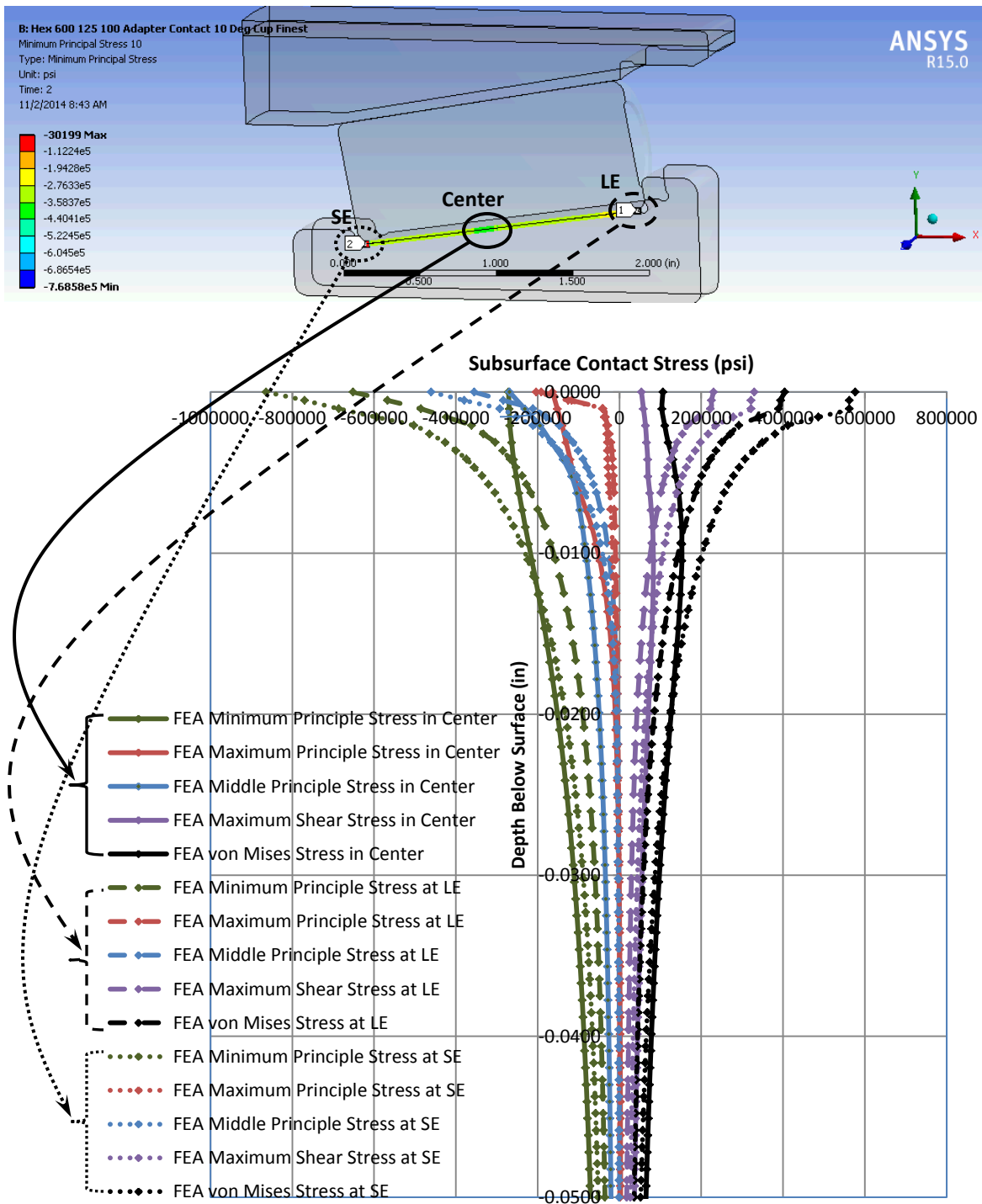
Figure 43: Subsurface Stress between Inner Raceway and Roller at Center, Large End (LE), and Small End (SE) of the Contact under 400% of Base Adapter Load

In addition to variations in load conditions, geometric modifications can also have an impact on surface stress results. As further illustration of how the novel finite element modeling methodology can be employed, two different bearing geometries were modeled under the same load. You can see that the load distribution along the semimajor axis of the Hertzian contact ellipse of the low crown geometry experiences edge loading while the high crown geometry does not (Figure 44). Also, as might be anticipated, the influence of the roller taper on surface stress results is more pronounced on the low crown geometry. If application loads remain constant, an optimized design for this load case may lie somewhere in between the low crown and high crown profile, in order to prevent hostile edge loading conditions while benefiting from maximum utilization of the total raceway length. Classical Hertzian contact theory, when compared to the length of the raceway in the design of interest, can be used to predict the occurrence of edge loading. However, in order to calculate the magnitude of surface stress and subsurface stress under these conditions, finite element or other numerical methods are necessary.
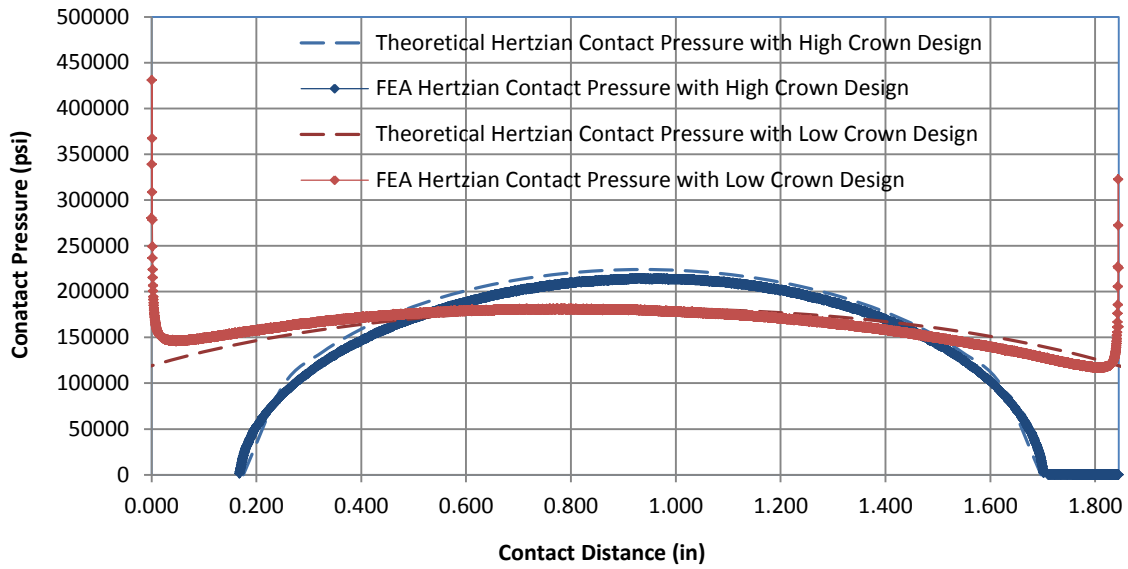
Figure 44: Hertzian Contact Pressure between Inner Raceway and Roller along the Semimajor axis of the Hertzian Contact Ellipse for Two Different Tapered Roller Bearing Geometries Exposed to the same Stribeck Load (Distance along the Roller Surface Starting from the Small End (SE) on the Left at 0.000 inches)

4.3 Conclusion and Future Work

Load scenarios presented in Chapter 4 validate the potential of the novel finite element method established. The wide range of possible applications for the method cannot be covered entirely, but a few general examples include: geometric design optimization, heat treat specification calculation, fatigue life criterion assessment, and assistance with bearing failure analyses. Further improvement to the tool is possible with more iterations of modeling. Computational expense will have to be balanced with accuracy for each application of the practical tool developed; however, a good foundation for future work has been accomplished. After demonstrating the accuracy of the method, it is interesting to consider what Lundberg and Palmgren would have done differently if they had access to finite element methods for the construction of probability of survival relationships and how the bearing industry would be different today?

With regards to accuracy of the finite element method, contact stabilization adjustments could be studies as well as the application of a mesh inflation layer, instead of partitioned surfaces for mesh refinement. Additionally, thinner sections of the inner and outer raceway could be tested in order to reduce the size of the model as long as additional deflection was not generated.

The accuracy of the Stribeck equation for tapered roller bearings with thin raceways has been questioned. Although outside of the scope of this paper, this

assumption has a huge impact on the results presented and further work related to the determination of railroad tapered roller bearing deflection under load is suggested. Once the individual roller load on a given design geometry is known, a practical tool for the determination of surface stresses in railroad bearings with different contact geometries and load conditions is at hand.

Literature Cited

Literature Cited

1. M.G. Dick BMW. Hertzian Contact Stress Modeling in Railcar Bearings using Finite Element Analysis. Presented at the ASME/RTD Bearing Steel Symposium, Chicago, IL, September 2007.

2. Harris TA. Essential Concepts of Bearing Technology, Fifth Edition. Hoboken: Hoboken : Taylor and Francis 2006.

3. Lundberg G, Palmgren A. Dynamic capacity of rolling bearings. 1948:8.

4. Zaretsky EV. Design for life, plan for death. Mach Des 1994;66:57-59.

5. Loesche T. New aspects in the realistic prediction of the fatigue life of rolling bearings. Wear 1989;134:357-375.

6. Ioannides E, Harris TA. New Fatigue Life Model for Rolling Bearings. Journal of Tribology 1985;107:367-377.

7. Ebert FJ. Fundamentals of Design and Technology of Rolling Element Bearings. Chinese Journal of Aeronautics 2010;23:123-136.

8. Harris TA, Yu WK. Lundberg-Palmgren fatigue theory: Considerations of failure stress and stressed volume. Journal of Tribology 1999;121:85-89.

9. Zaretsky EV. In search of a fatigue limit: A critique of ISO Standard 281:2007. TRIBOLOGY & LUBRICATION TECHNOLOGY; Tribol.Lubr.Technol. 2010;66:30-+.

10. Lundberg G, Palmgren A. Dynamic capacity of roller bearings. Engineers' Digest (British Edition) 1952;13:217-219.

11. American Bearing Manufacturers Association. Load Ratings and Fatigue Life for Roller Bearings. 2011.

12. Zaretsky EV, Branzai EV. Effect of rolling bearing refurbishment and restoration on bearing life and reliability. Tribol Trans 2005;48:32-44.

13. Harris TA, McCool JI. On the accuracy of rolling bearing fatigue life prediction. 1995:13pp-13pp.

14. Harris TA. Advanced Concepts of Bearing Technology, Rolling Bearing Analysis, Fifth Edition. Hoboken: Hoboken : Taylor and Francis 2006.

15. Roller Bearing Manual Section H-II. In Anonymous Manual of Standards and Recommended Practices. Washington, DC: Association of American Railroads 2012.

16. Guo Y, Parker RG. Stiffness matrix calculation of rolling element bearings using a finite element/contact mechanics model. Mechanism and Machine Theory 2012;51:32-45.

17. Cretu S, Bercea I, Mitu N. Dynamic analysis of tapered roller bearing under fully flooded conditions Part 1: theoretical formulation. Wear 1995;188:1-10.

18. Wilson BM, Dick MG. Development of a predictive life tool for tapered roller bearings using measured residual stress and retained austenite data. Powder Diffraction 2008;23:118-20.

19. Nagatani H. Improved method of roller bearing fatigue life prediction under edge loading conditions. Tribol Trans 2010;53:695-702.

20. Kumar KS, Tiwari R, Prasad PVV. An optimum design of crowned cylindrical roller bearings using genetic algorithms. Journal of Mechanical Design 2009;131:051011 (14 pp.).

21. Krzeminski-Freda H, Warda B. Correction of the roller generators in spherical roller bearings. Wear 1996;192:29-39.

22. Broszeit E, Adelmann J, Zwirlein O. Influence of internal stresses on the stressing of material in components subjected to rolling-contact loads. Zeitschrift fur Werkstofftechnik 1985;16:19-24.

23. Andreason S. Load Distribution in a Taper Roller Bearing Arrangement Considering Misalignment. Tribology (London) 1973;6:84-92.

24. Broszeit E, Zwirlein O. Internal stresses and their influence on material stresses in Hertzian contacts-calculations with different stress hypotheses. Transactions of the ASME Journal of Tribology 1986;108:387-93.

25. Gupta PK. On the dynamic of a tapered roller bearing. Journal of Tribology 1989;111:278-287.

26. Johnson KL(. Contact mechanics. Cambridge Cambridgeshire] ; New York: Cambridge Cambridgeshire ; New York : Cambridge University Press; Cambridge : Cambridge University Press, c1985 1987.

27. Glaister P. Intersecting Chords Theorem: 30 Years on. Mathematics in School 2007;36:22-22.

28. Yongqi Z, Qingchang T, Kuo Z, Jiangang L. Analysis of Stress and Strain of the Rolling Bearing by FEA method. Physics Procedia 2012;24:19-24.

29. Knudsen E. Finite Element Modeling of a Cylindrical Contact Using Hertzian Assumptions. 2002:5p.

30. Yastrebov VA. Numerical Methods in Contact Mechanics. Hoboken: Hoboken : Wiley 2013.

Appendices

Appendix A: Theoretical Stribeck Equation Calculations

Static roller load distributions in bearing assemblies are commonly calculated using the Stribeck equations [2]. Before roller load distribution calculations can occur, load deflection relationships for the given bearing design must be developed using Hertzian contact theory. For the bearing load distribution studies conducted as background information in this paper, it was assumed that the impact of inertial forces and frictional forces were negligible.

According to Stribeck, roller load approximations may be calculated as follows. The contact normal load per roller in the direction normal to the contacting surfaces Q, can be related to contact deflection in the direction normal to the surfaces through

$$Q = (\delta_i + \delta_o)^n \left[\frac{1}{(\frac{1}{K_i})^{1/n} + (\frac{1}{K_o})^{1/n}} \right]^n \tag{50}$$

where δ_o is the contact deflection of the outer ring contact and δ_i is the contact deflection of the inner ring contact. In equation (50), n is 3/2 for point contacts and 10/9 for line contacts. With regards to the load deflection factors K_i and K_o, these have previously been determined to be equivalent to

$$2.15 x 10^5 (\textstyle\sum \rho)^{-1/2} (\delta^*)^{-3/2} \tag{51}$$

93

for steel bearing surfaces experiencing point contact and

$$8.06x10^4 (l)^{8/9}$$ (52)

for steel bearing surfaces experiencing line contact [2]. Where $\sum \rho$ is the curvature sum for the contacting surfaces, δ^* is the dimensionless contact deformation calculated using Hertzian contact theory, and l is the effective roller length.

Once a relationship between contact normal load and deflection has been established for contacting surfaces, overall bearing deflection behavior may be analyzed. For rigidly supported bearings, radial deflection at each given angular roller position φ, is

$$\delta_\varphi = \delta_{max} \left[1 - \frac{1}{\left(1 - \frac{P_d}{2\delta_r} \right)} (1 - cos(\varphi)) \right]$$ (53)

and the load at each roller position is

$$Q_\varphi = Q_{max} \left[1 - \frac{1}{\left(1 - \frac{P_d}{2\delta_r} \right)} (1 - cos(\varphi)) \right]^n .$$ (54)

In equations (53) and (54), P_d is the diametric clearance and δ_r is the ring radial shift. In order for static equilibrium to be achieved, the sum of the individual roller loads in the vertical direction must be equal to the total vertical load applied to the bearing. This relationship can be expressed as

$$F_r = Q_{max} \sum_{\varphi=0}^{\varphi=\pm\varphi_l} \left[1 - \frac{1}{\left(1 - \frac{P_d}{2\delta_r} \right)} (1 - cos(\varphi)) \right]^n cos(\varphi)$$ (55)

or

$$F_r = \frac{Z*Q_{max}}{2\pi} \int_{-\varphi_l}^{+\varphi_l} \left[1 - \frac{1}{\left(1-\frac{P_d}{2\delta_r}\right)} \left(1 - cos(\varphi)\right)\right]^n cos(\varphi)d\varphi \qquad (56)$$

where

$$\varphi_l = cos^{-1}\left(\frac{P_d}{2\delta_r}\right) \qquad (57)$$

is the angular extent of the load zone,

$$Q_{max} = (\delta_i + \delta_o)^n \left[\frac{1}{(\frac{1}{K_i})^{1/n}+(\frac{1}{K_o})^{1/n}}\right]^n \Bigg|_{\varphi=0} \qquad (58)$$

is the maximum roller load, and Z is the number of rollers. Knowing that the maximum roller load will occur at the top dead center position at $\varphi = 0$, the sum of the inner raceway and outer raceway deflections can be related to radial ring shift and clearance by

$$\delta_i + \delta_o = \delta_r + \frac{1}{2}P_d. \qquad (59)$$

If radial clearance and total bearing load are known, the roller load distribution in an assembly may be determined by adjusting radial ring shift δ_r until the condition of equation (59) is achieved. Then, using equation (54), the other individual roller loads Q_φ, within the angular extent of the contact zone φ_l, may be determined.

Appendix B: Derivation of Radius of Curvature to Crown Height Relationship for Tapered Roller Bearings

It is common in the tapered roller bearing industry to use crown height, instead of radius of curvature or curvature, to identify raceway and roller elliptical contact profile geometry. The relationship between crown height and radius of curvature in equation (39) is derived from the Intersecting Chords Theorem

$$AP * DP = BP * CP \qquad (60)$$

related to the geometric condition shown in Figure 45.
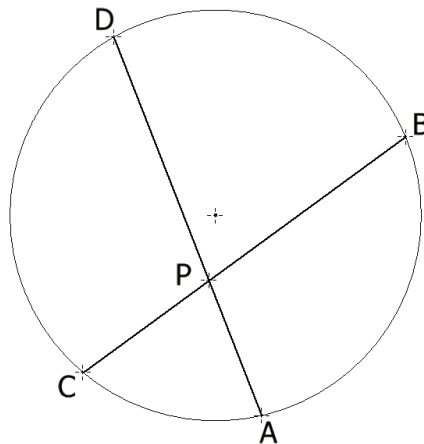
Figure 45: Intersecting Chords Theorem for Circle

Considering equation (55) and Figure 8, the variables in equation (55) may be replaced with the detailed bearing geometry discussed in Chapter 2 and shown below in Figure 46. This substitution results in the relationship

$$h_c * (2r - h_c) = \frac{1}{2}l_c * \frac{1}{2}l_c \tag{61}$$

which can easily be rearranged to derive the relationship in equation (39).
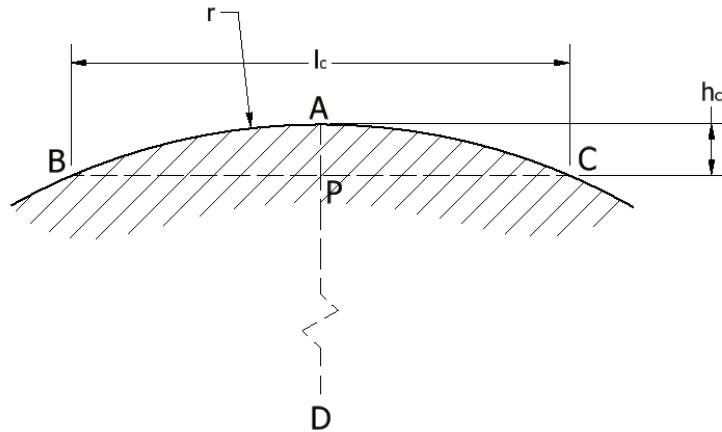
Figure 46: Relationship between Radius of Curvature r, Crown Height h_c, and Center Span Crown Length l_c using the Intersecting Chords Theorem

Appendix C: Proof that the Force between the Outer Raceway and Roller is Equal to that between the Roller and Inner Raceway when the Flange Angle is Equal to the Average of the Inner and Outer Raceway Angles

The following proof will demonstrate that the force transferred from the cup to the roller is the same as that transferred from the roller to the cone raceway in common tapered railroad bearing geometries if the relationship of equation (45) applies to the bearing design. Beginning with the summation of roller forces in the radial direction

$$-Q\cos(\theta_o) + Q_i\cos(\theta_i) - Q_f\sin(\theta_f) = 0 \tag{62}$$

and the summation of roller forces in the lateral direction

$$-Q\sin(\theta_o) + Q_i\sin(\theta_i) + Q_f\cos(\theta_f) = 0, \tag{63}$$

as shown in Figure 47, the relationship

$$Q_i = \frac{Q\cos(\theta_o) + Q_f\sin(\theta_f)}{\cos(\theta_i)} \tag{64}$$

can be established   as well as equation (48) for Q_f by substituting equation (63) into equation (62). Replacing Q_f in equation (61) with equation (48) results,

$$Q_i = Q\left[\frac{\cos(\theta_o)}{\cos(\theta_i)} + \frac{\sin(\theta_o)\sin(\theta_f) - \cos(\theta_o)\sin(\theta_f)\tan(\theta_i)}{\cos(\theta_f)\cos(\theta_i) + \sin(\theta_f)\sin(\theta_i)}\right] \tag{65}$$

forms a relationship between Q and Q_i which can be simplified by addition of the fractions as

$$Q_i = Q\left[\frac{\cos(\theta_o)\cos(\theta_f) + \sin(\theta_o)\sin(\theta_f)}{\cos(\theta_f)\cos(\theta_i) + \sin(\theta_f)\sin(\theta_i)}\right]. \tag{66}$$

Then, utilizing the trigonometric sum and difference identity

$$\cos(A - B) = \cos(A)\cos(B) + \sin(A)\sin(B) \tag{67}$$

equation (65) can be simplified to equation (46). Furthermore, it can be seen through substitution into equation (46), that if equation (45) applies to the bearing design of interest that the force transferred from the cup to the roller is the same as that transferred from the roller to the cone raceway and correspondingly Q_i is equal to Q.
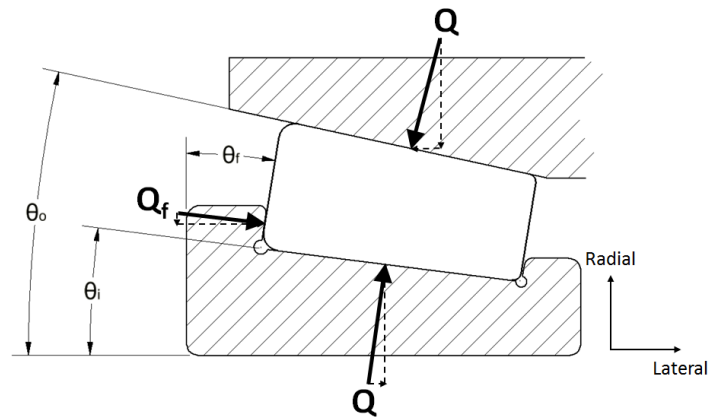
Figure 47: Summation of Forces on Tapered Roller Geometry Including Force Components in Radial and Lateral Directions

Appendix D: Material Properties Associated with Structure Steel Utilized in Finite Element Simulations

Table 4: Material Properties used in Finite Element Model for all Components

Material Property	Value
Young's Modulus (psi)	2.9008E+07
Poisson's Ratio	0.3
Bulk Modulus (psi)	2.4173E+07
Shear Modulus (psi)	1.1157E+07

Appendix E: Additional Software Settings for Finite Element Analyses

Table 5:   Additional Settings in Ansys, Inc. Software used for Primary Finite Element Analysis

Finite Element Parameter	Value
Geometric Settings:	
Nonlinear Effects (all bodies)	Yes
General Contact Settings:	
Tolerance Value	.02 inches
Face/Face	Yes
Face/Edge	Yes
Edge/Edge	Yes
All Raceway Contact Settings:	
Type	Frictionless
Behavior	Asymmetric
Formulation	Augmented Lagrange
Detection Method	Nodal-Projected Normal from Contact
Stabilization Damping Factor	1
Pinball Radius	.02 inches
Time Step Controls	Automatic Bisection
Interface Treatment	Adjust to Touch (Cone Back Rib), Add Offset,

	Ramped Effects (All Others)
Mesh Settings:	
Relevance	100
Relevance Center	Fine
Initial Size Speed	Active Assembly
Smoothing	High
Transition	Slow
Span Angle Center	Medium
Shape Checking	Standard Mechanical
Analysis Settings:	
Initial Substeps	10
Minimum Substeps	50
Maximum Substeps	1
Large Deflections	Off

VITA

Michael Allan Mason was born in Cumberland, Maryland on February 18th, 1982, the son of Bruce Allan Mason and Susan Elizabeth Will. He attended Atlee High School in Mechanicsville, Virginia before attending Virginia Polytechnic Institute and State University in Blacksburg, Virginia where he received a Bachelor of Science in Mechanical Engineering in 2005. Immediately after completing his undergraduate degree, he began working for Amsted Rail Company, Inc. in their Product Engineering department as a Product Development Engineer, where he acquired six patents related to railroad bearing design and served on the Roller Bearing Manufacturers Engineering Committee of the Association of American Railroads. He enrolled in the School of Engineering at Virginia Commonwealth University in 2011 and is currently serving as the Director of Product Development and Performance Engineering, Bearings at Amsted Rail where he is heavily involved in development of railroad bearings, the resolution of bearing related issues around the world, and driving improvements related to railroad maintenance regulations.